Molecular Neurobiology (2019) 56:4322–4345
https://doi.org/10.1007/s12035-018-1376-2

Heterozygous *Meg2* Ablation Causes Intraocular Pressure Elevation and Progressive Glaucomatous Neurodegeneration

Jacqueline Reinhard[1] · Susanne Wiemann[1] · Stephanie C. Joachim[2] · Marina Palmhof[2] · Julia Woestmann[1] · Bernd Denecke[3] · Yingchun Wang[4] · Gregory P. Downey[5,6] · Andreas Faissner[1]

Received: 15 April 2018 / Accepted: 28 September 2018 / Published online: 12 October 2018

Abstract

Glaucomatous neurodegeneration represents one of the major causes of irreversible blindness worldwide. Yet, the detailed molecular mechanisms that initiate optic nerve damage and retinal ganglion cell (RGC) loss are not fully understood. Members of the protein tyrosine phosphatase (PTP) superfamily are key players in numerous neurodegenerative diseases. In order to investigate the potential functional relevance of the PTP megakaryocyte 2 (Meg2) in retinal neurodegeneration, we analyzed *Meg2* knockout (KO) and heterozygous (HET)—synonym *protein-tyrosine phosphatase non-receptor type 9* (*Ptpn9*)—mice. Interestingly, via global microarray and quantitative real-time PCR (RT-qPCR) analyses of *Meg2* KO and HET retinae, we observed a dysregulation of several candidate genes that are highly associated with retinal degeneration and intraocular pressure (IOP) elevation, the main risk factor for glaucoma. Subsequent IOP measurements in *Meg2* HET mice verified progressive age-dependent IOP elevation. Ultrastructural analyses and immunohistochemistry showed severe optic nerve degeneration accompanied by a dramatic loss of RGCs. Additionally, HET mice displayed reactive micro-/macrogliosis and early activation of the classical complement cascade with pronounced deposition of the membrane attack complex (MAC) in the retina and optic nerve. When treated with latanoprost, significant IOP lowering prevented RGC loss and microglial invasion in HET mice. Finally, electroretinogram (ERG) recordings revealed reduced a- and b-wave amplitudes, indicating impaired retinal functionality in *Meg2* HET mice. Collectively, our findings indicate that the heterozygous loss of *Meg2* in mice is sufficient to cause IOP elevation and glaucomatous neurodegeneration. Thus, *Meg2* HET mice may serve as a novel animal model to study the pathomechanism involved in the onset and progression of glaucoma.

Keywords Glaucoma · Intraocular pressure elevation · Mouse model · Neurodegeneration · Protein tyrosine phosphatase Meg2 · Retina

Electronic supplementary material The online version of this article (https://doi.org/10.1007/s12035-018-1376-2) contains supplementary material, which is available to authorized users.

✉ Andreas Faissner
andreas.faissner@rub.de

[1] Department of Cell Morphology and Molecular Neurobiology, NDEF 05/594, Faculty of Biology and Biotechnology, Ruhr-University Bochum, Universitätsstrasse 150, 44780 Bochum, Germany

[2] Experimental Eye Research Institute, University Eye Hospital, Ruhr-University Bochum, In der Schornau 23-25, 44892 Bochum, Germany

[3] Interdisciplinary Centre for Clinical Research, RWTH Aachen University, Pauwelsstrasse 30, 52074 Aachen, Germany

[4] Division of Respirology, Department of Medicine, University of Toronto and Toronto General Hospital Research Institute of the University Health Network, 610 University Avenue, Toronto, ON M5S 1A8, Canada

[5] Division of Pulmonary Sciences and Critical Care Medicine, Departments of Medicine and Immunology and Microbiology, University of Colorado, Aurora, CO 80045, USA

[6] Division of Pulmonary, Critical Care and Sleep Medicine, Departments of Medicine, Pediatrics and Biomedical Research, National Jewish Health, 1400 Jackson Street, Denver, CO 80206, USA

Introduction

Glaucoma is one of the leading causes of visual impairment and irreversible blindness, currently affecting more than 60 million people worldwide, but the number of people with glaucoma might even increase to more than 111 million in 2040 [1]. Overall, glaucoma is a neurodegenerative and multifactorial disease that is characterized by optic nerve damage as well as RGC apoptosis [2, 3]. Primary open-angle glaucoma (POAG) represents the most common form of glaucoma, and intraocular pressure (IOP) elevation constitutes as the main risk factor [4]. Several studies indicate that macroglial response influences glaucoma pathogenesis [5, 6]. Additionally, microglial and complement activation seem to play a key role in this disease [7–9]. However, the exact underlying molecular mechanisms involved in glaucomatous neurodegeneration are not yet fully understood.

The phosphorylation of proteins on tyrosine residues represents a critical mechanism for the control of numerous cellular processes. Phosphate is selectively removed from tyrosines by a family of enzymes known as protein tyrosine phosphatases (PTPs) [10, 11]. The dephosphorylation of proteins on tyrosine residues via members of the PTP superfamily is a critical factor for the outcome of numerous diseases [12–15]. Moreover, PTP members represent crucial signaling molecules in the regulation of the immune response [16]. While members of the PTP superfamily also coordinate many aspects in the central nervous system (CNS), the expression patterns and potential functional roles of PTPs in the retina still remain poorly investigated [17, 18].

We previously reported the identification and expression of various PTPs in the developing mouse visual system [19, 20]. In the present study, we focused on the ocular phenotype of *megakaryocyte 2* (*Meg2*)-deficient mice. Meg2 represents an intracellular PTP, which was originally cloned from a megakaryocytic cell line [21]. The PTP-Meg2 has been most extensively studied in the hematopoietic system, where the protein is thought to function as a key regulator for differentiation at several branching points within the hematopoietic lineage [22, 23]. Furthermore, Meg2 is associated with vesicle-trafficking proteins and promotes intracellular secretory vesicle fusion [24–27].

The function of Meg2 in the CNS is not well known, although evidence suggests that the protein plays an important role in some aspects of neural development [28]. Most recently, it was shown that Meg2 controls neurite growth and differentiation of cortical neurons [29]. A crucial role of Meg2 during embryonic CNS development is underscored by the prominent expression of this phosphatase within the brain and the severe phenotype reported for *Meg2* KO mice [26]. Indeed, PTP-Meg2 KO mice exhibit severe neurodevelopmental defects including exencephaly and a reduced brain size. In addition, PTP-Meg2 is a CRAL-TRIO (Sec14) domain-containing protein. Mutations in several Sec14 domain-containing proteins result in the onset of human pathologies including neurodegeneration, blindness, and cancer [30].

In the present study, we comprehensively characterized the ocular phenotype of *Meg2*-deficient mice. As revealed by a global microarray approach and RT-qPCR analyses, we found that *Meg2* KO and heterozygous (HET) mice display a dysregulation of various glaucoma and retinal degeneration-associated genes. *Meg2* HET mice show IOP elevation followed by severe optic nerve and retinal degeneration.

Materials and Methods

Mice

All animal experiments were conducted in compliance with the "Association for Research and Vision and Ophthalmology" statement for the use of animals in ophthalmic and vision research and were approved by the ethics committee for animal experiments by the state North-Rhine Westphalia, Germany. Analyses were performed using age-matched *Meg2* KO, HET [26], and C57BL/6NTac (mutant background strain) WT littermates. The *Meg2* mutant was kindly provided by G. P. Downey.

RNA Isolation, Complementary DNA Synthesis, Multiplex PCR, and RT-qPCR

For RNA isolation, retinae and optic nerves were prepared, frozen in liquid nitrogen, and stored at − 70 °C. Total RNA extraction from retinae and optic nerves was performed according to the manufacturer's instructions as described previously [31, 32]. RNA quality and quantity were analyzed with a BioSpectrometer® (Eppendorf). Using a cDNA synthesis kit (Thermo Fisher Scientific), 1 μg total RNA was used for reverse transcription. Genomic DNA was isolated using the DirectPCR® Lysis Reagent (Peqlab). Multiplex PCR analyses for genotyping were performed as described before [26] with the JumpStart™ Tag DNA polymerase (Sigma-Aldrich). Oligonucleotides were designed using Primer3 (http://frodo.wi.mit.edu/) or ProbeFinder (Roche; Table S1) software. RT-qPCR and statistical analyses were performed as described previously [32, 33]. Relative expression variations were evaluated by a pairwise fixed reallocation and randomization test using REST© software [34].

Affymetrix GeneChip Analyses and Data Acquisition

For microarray analyses, total RNA was extracted from retinae of WT and *Meg2* KO mice at postnatal day 0 using the RNeasy mini kit (Qiagen). Gene expression in retinae of WT and *Meg2* KO mice was analyzed by Affymetrix® GeneChip® MouseGene1.0 ST (Affymetrix) in independent triplicates.

Probes for the arrays were prepared and hybridized according to the Ambion whole transcript expression and the Affymetrix whole transcript terminal labeling and control kit manuals. Image data were analyzed using the Affymetrix GeneChip™ Command Console software (Affymetrix). Microarray expression analyses and comparison were conducted using Bioconductor1 packages under R2 background correction [35]. For normalization, the RMA algorithm was used [36]. Only those genes that were expressed higher than threefold over the negative control were further analyzed. Values of ≥ 0.2 log or ≤− 0.2 were used as cutoff for up- and downregulation. The Affymetrix GeneChip data have been deposited in NCBI's Gene Expression Omnibus and are accessible through GEO Series accession number GSE119246.

Intraocular Pressure Measurements

The IOP of WT and HET mice was measured with a rebound tonometer (TonoLab) as described previously [37]. Per eye, 10 readings were averaged, and mean values were calculated. IOP measurements of randomized mixed WT and HET groups were usually performed in the morning.

Latanoprost Treatment

IOP was evaluated in WT and HET mice between 7 and 13 weeks. Following significant IOP elevation in HET mice at 10 weeks, some WT and HET animals were topically treated daily with the prostaglandin analogue latanoprost (0.005% Xalatan®; Pfizer Pharmacia). Untreated WT and HET mice served as control groups. At 14 weeks, retinal flat-mounts were analyzed immunohistochemically.

Hematoxylin-Eosin Staining and (Immuno-) Histological Procedures

After removal, eyes and optic nerves were fixed in 4% paraformaldehyde and embedded in Tissue-Tek for cross-sectioning using a cryostat (CM3050 S, Leica). Additionally, some fixed eyes were dissected as flat-mounts. Hematoxylin-eosin (H&E) staining procedure of retinal/eye sections was performed using a H&E kit (Thermo Fisher Scientific) as described by the manufacturer's protocol. For central corneal thickness (CCT; orientation to the lens central: 0°) measurements, two horizontal eye sections in a medial and peripheral section area per animal were analyzed. For immunohistochemistry, horizontal retinal and longitudinal optic nerve cryo-sections as well as retinal flat-mounts were blocked in blocking solution containing 1–3% normal goat or donkey serum (Dianova), 1% bovine serum albumin, and 0.5–2% Triton™ X-100 (Sigma-Aldrich) in phosphate-buffered saline at room temperature for 1 h. Then, tissue was incubated in an antibody solution (blocking solution and primary antibodies) for 12–24 h (Table S2). Following further washing steps in phosphate-buffered saline, cryo-sections and flat-mounts were incubated in a secondary antibody solution (blocking solution without Triton™ X-100) overnight. Appropriate secondary antibodies were obtained from Dianova (Table S2). Cell nuclei were visualized using TO-PRO®-3 iodide (1:400; Thermo Fisher Scientific). To evaluate the numbers of retinal ganglion cells (RGCs) and microglia in retinal flat-mounts, brain-specific homeobox/POU domain protein 3a (Brn3a)$^+$ and ionized calcium-binding adapter molecule 1 (Iba1; alias: allograft inflammatory factor 1)$^+$ cells were quantified in the peripheral and central retina (× 200 magnification; 8 counting windows/retinal flat-mount/animal; 2 counting windows from each retinal quadrant). For circumference and area size measurements of Brn3a$^+$ nuclei, 160 cells (× 400 magnification; 16 counting windows; 4 counting windows from each retinal quadrant; 10 cells/counting window) were analyzed. For retinal section analyses, pictures were taken as described previously [32]. Inducible nitric oxide synthase (iNOS$^+$), Iba1$^+$, and membrane attack complex (MAC)$^+$ cells were quantified in retinal sections (3–4 counting windows/retina; 2 retinae/animal). Immunoreactive cells were also counted in optic nerve sections (3 counting windows/optic nerve; 2 optic nerves/animal). Staining signal areas (3–4 counting windows/retina; 2 retinae/animal) of glial fibrillary acidic protein (GFAP), neurofilament-200 (NF-200), and vimentin were analyzed using ImageJ software (National Institutes of Health) as described previously [31, 32, 38]. Images were transferred into grayscale pictures, and background subtraction and upper and lower threshold were determined. For transmission electron microscopy (TEM; Phillips EM-410), optic nerves were fixed in 2.5% glutaraldehyde in cacodylate buffer (pH 7.38) at 4 °C overnight, and rinsed in 0.1 M cacodylate buffer. Tissue samples were incubated in 2% osmium tetroxide solution, dehydrated in graded concentrations of ethanol/epon-propylene oxide, and embedded in epon. Ultrathin sections (80 nm) were prepared, and images were captured from myelinated, most proximal regions of the optic nerve.

Microscopy and Image Capture

Brightfield H&E images were captured using the Axio Zoom V16 (Zeiss). Fluorescent specimens were captured with the confocal laser scanning microscope LSM 510 META (Zeiss). Images were processed using Adobe Photoshop and Illustrator software (Adobe Systems).

Electroretinogram Recordings

Scotopic full-field flash electroretinogram (ERG) recordings (HMsERG system, OcuScience) were performed as described previously [37]. Single-light flash responses were recorded in dark-adapted WT and HET mice. For data analyses, a low-

Table 1 Most prominently up- and downregulated genes in the *Meg2* KO compared to the WT P0 retinae as revealed by microarray analyses ($n = 2–3$)

Gene symbol	Gene title	Affymetrix transcript cluster ID	Average log2-fold	SEM log2-fold	*p* value	Biological process
Downregulated genes						
Adpgk	***ADP-dependent glucokinase***	**10585860**	**−0.37**	**0.08**	**0.0467**	**Carbohydrate metabolic process/glycolysis**
Ptpn9 (Meg2)	***Protein tyrosine phosphatase, non-receptor type 9***	**10585610**	**−0.58**	**0.12**	**0.0049**	**Protein amino acid dephosphorylation/dephosphorylation**
Upregulated genes						
Bgn	***Biglycan***	**10600169**	**0.59**	**0.07**	**0.0082**	**Peptide cross-linking via chondroitin 4-sulfate glycosaminoglycan**
C1qb	*Complement component 1, q subcomponent, beta poly-peptide*	10517508	0.47	0.17	0.0589	Immune response/complement activation/classical pathway/innate immune response
Cd34	***CD34 antigen***	**10352905**	**0.68**	**0.07**	**0.0064**	**Cell adhesion/leukocyte migration**
Hif3a	*Hypoxia-inducible factor 3, alpha subunit*	10560329	0.90	0.38	0.1180	Response to hypoxia/transcription/regulation of transcription, DNA-dependent/transcription from RNA polymerase II promoter/signal transduction/regulation of transcription
Igfbp7	***Insulin-like growth factor-binding protein 7***	**10530841**	**0.87**	**0.11**	**0.0102**	**Regulation of cell growth/cell adhesion**
Lmo2	*LIM domain only 2*	10474201	0.50	0.27	0.2408	Negative regulation of erythrocyte differentiation
Mt1	*Metallothionein 1*	10574027	0.48	0.18	0.1631	Cellular metal ion homeostasis/cellular zinc ion homeostasis/nitric oxide-mediated signal transduction/detoxification of copper ion
Mt2	*Metallothionein 2*	10574023	0.95	0.27	0.3246	Cellular zinc ion homeostasis/nitric oxide-mediated signal transduction/detoxification of copper ion
Per1	*Period homolog 1 (Drosophila)*	10377439	0.69	0.30	0.2404	Transcription/regulation of transcription, DNA-dependent/signal transduction/circadian rhythm/negative regulation of transcription/rhythmic process
Ppp1r3c	*Protein phosphatase 1, regulatory (inhibitor) subunit 3C*	10467206	0.90	0.43	0.1565	Carbohydrate metabolic process/glycogen metabolic process/glycogen biosynthetic process/protein targeting
Rbp4	*Retinol-binding protein 4, plasma*	10467319	0.64	0.25	0.0849	Eye development/gluconeogenesis/transport/spermatogenesis/spermatogonial cell division/male gonad development/embryonic development/lung development/response to insulin stimulus/retinol transport/retinol metabolic process/retinal metabolic process/embryonic organ morphogenesis/embryonic skeletal system development/cardiac muscle tissue development/female genitalia morphogenesis/detection of light stimulus involved in visual perception/positive regulation of immunoglobulin secretion/retina development in camera-type eye/negative regulation of cardiac muscle cell proliferation/embryonic retina morphogenesis in camera-type eye/uterus development/vagina development/urinary bladder development/heart trabecula formation
Slc15a2	*Solute carrier family 15 (H+/peptide transporter), member 2*	10439321	1.76	0.59	0.0535	Transport/oligopeptide transport/protein transport
Srgn	***Serglycin***	**10369615**	**0.61**	**0.12**	**0.0229**	**Ossification/apoptosis/mast cell secretory granule organization/T cell secretory granule organization/maintenance of protease**

Table 1 (continued)

Gene symbol	Gene title	Affymetrix transcript cluster ID	Average log2-fold	SEM log2-fold	*p* value	Biological process
						location in mast cell secretory granule/maintenance of granzyme B location in T cell secretory granule/negative regulation of cytokine secretion/protein maturation by peptide bond cleavage
Unc13c	***Unc-13 homolog C (C. elegans)***	**10594965/ 10594967/ 10594948/ 10594973/ 10594963**	**0.65**	**0.14**	**0.0004**	**Exocytosis/intracellular signaling cascade/synaptic transmission**

Dysregulated genes with a p value < 0.05 are shown in bold

pass filter (150 Hz) was applied before evaluating a- and b-wave amplitudes.

Statistical Evaluation

Data of the immunohistological analyses, IOP, and ERG measurements were statistically evaluated by the unpaired Student's *t* test or one-way ANOVA followed by Tukey's post hoc test using Statistica software (StatSoft). Values are shown as mean ± standard error of the mean (SEM) and/or standard deviation (SD). p values of < 0.05 were considered statistically significant.

Results

Dysregulation of Retinal Degeneration-Associated Genes in *Meg2* Knockout and Heterozygous Retinae

In order to determine the molecular changes that resulted from Meg2 loss and to identify differentially regulated genes in the *Meg2* KO retina, we performed global gene expression analyses using a microarray approach. Owing to the early postnatal lethality of the KO mice, these analyses were performed at postnatal stage 0. At this point in time, more than 17,000 genes were expressed. Genes that were most prominently dysregulated are shown in Table 1. Transcripts found to be ≥ 0.2 or ≤ − 0.2 log2-fold up- or downregulated are listed in Table 2. Differentially expressed genes were also investigated by pathway analyses using Kyoto Encyclopedia of Genes and Genomes (KEGG) software (http://www.genome.jp/kegg/pathway.html, Stratagene; Table S3). Most interestingly, we observed dysregulation of several genes known to be differentially expressed in response to retinal neurodegeneration, which includes genes related to apoptosis, cellular stress, excitotoxicity, immune activation, neurotrophic signaling, oxidative stress, and loss of synaptic integrity [9, 39]. Additionally, dysregulation of the identified genes was reported in strong correlation with ocular hypertension and retinal diseases such as glaucoma.

Due to these findings and the lethality of *Meg2* KO mice, we next analyzed potential expression changes of various identified candidate genes in adult *Meg2* HET retinae. RT-qPCR analyses revealed a significant downregulation of *Adpgk* (0.80-fold; $p = 0.044$), while for *Bgn* (1.24-fold; $p = 0.030$), a significant upregulation was found in the HET compared to the WT retinae (Figure S1; Table S4). This dysregulation is consistent with the findings observed in the postnatal *Meg2* KO retinae (Table 1). In contrast, no dysregulation was observed for *Cd34* (1.30-fold; $p = 0.173$), *Igfbp7* (1.34-fold; $p = 0.109$), *Srgn* (1.16-fold; $p = 0.247$), and *Unc13c* (1.10-fold; $p = 0.188$).

Additionally, we analyzed the messenger RNA (mRNA) expression of the selected, most interesting genes: *Cacna1f*, *Cerkl*, *Grid2*, *Gstm3*, and *Igfbp3* in HET and WT retinae by RT-qPCR (Figure S1; Table S4). A comparable expression was observed for *Cacna1f* (1.02-fold; $p = 0.843$), *Cerkl* (1.02-fold; $p = 0.835$), and *Gstm3* (0.94-fold; $p = 0.225$), while a significant upregulation was found for *Grid2* (1.37-fold; $p = 0.014$) and *Igfbp3* (1.66-fold; $p = 0.021$). In sum, our comprehensive expression analyses verified a dysregulation of various glaucoma and retinal degeneration-associated candidate genes in the *Meg2* HET retinae.

Meg2 HET Mice Exhibit IOP Elevation

As IOP elevation is a main risk factor for glaucomatous retinal neurodegeneration, we performed IOP measurements in HET and WT littermates (Fig. 1a). At 6 weeks, we observed no significant differences in the IOP of WT (10.20 ±

Table 2 List of ≥ 0.2 or ≤− 0.2 log2-fold up- and downregulated genes in the *Meg2* KO compared to the WT P0 retinae as revealed by microarray analyses ($n = 2–3$)

Gene symbol	Gene title	Affymetrix transcript cluster ID	Average log2-fold	SEM log2-fold	*p* value	Biological process
Downregulated genes						
Acot9	***Acyl-CoA thioesterase 9***	**10602739**	**− 0.22**	**0.08**	**0.0099**	–
Apip	***APAF1 interacting protein***	**10474159**	**− 0.25**	**0.08**	**0.0004**	**Apoptosis/negative regulation of apoptosis**
Arhgef19	*Rho guanine nucleotide exchange factor (GEF) 19*	10509947	− 0.21	0.12	0.2688	Intracellular signaling cascade/regulation of Rho protein signal transduction
Armc2	*Armadillo repeat containing 2*	10368881	− 0.23	0.11	0.1757	–
Asns	*Asparagine synthetase*	10543067	− 0.21	0.09	0.1187	Asparagine biosynthetic process/glutamine metabolic process/metabolic process/amino acid biosynthetic process
Atoh8	*Atonal homolog 8 (Drosophila)*	10545372	− 0.21	0.10	0.1629	Transcription/regulation of transcription, DNA-dependent/multicellular organismal development/nervous system development/cell differentiation/regulation of transcription
Atp5k	*ATP synthase, H+ transporting, mitochondrial F1F0 complex, subunit e*	10532164	− 0.22	0.12	0.2262	ATP biosynthetic process/transport/ion transport/ATP synthesis-coupled proton transport/proton transport
ATP6	*ATP synthase F0 subunit 6*	10598085	− 0.21	0.14	0.3571	ATP biosynthetic process/transport/ion transport/ATP synthesis-coupled proton transport/proton transport
Cacna1f	***Calcium channel, voltage-dependent, alpha 1F subunit***	**10598309**	**− 0.23**	**0.08**	**0.0359**	**Transport/ion transport/calcium ion transport/cellular calcium ion homeostasis/axonogenesis/visual perception/dendrite morphogenesis/response to stimulus**
Cenpk	*Centromere protein K*	10406968	− 0.21	0.15	0.3657	Positive regulation of transcription from RNA polymerase II promoter
Cerkl	***Ceramide kinase-like***	**10484261**	**− 0.32**	**0.11**	**0.0042**	–
Cetn4	***Centrin 4***	**10497894**	**− 0.21**	**0.08**	**0.0417**	–
Cfl2	*Cofilin 2, muscle*	10400350	− 0.21	0.14	0.3492	–
Ddx11	***DEAD/H (Asp-Glu-Ala-Asp/His) box polypeptide 11 (CHL1-like helicase homolog, Saccharomyces cerevisiae)***	**10446441**	**− 0.32**	**0.12**	**0.0407**	**Nucleobase, nucleoside, nucleotide and nucleic acid metabolic process/cell cycle**
Dus2l	*Dihydrouridine synthase 2-like (SMM1, S. cerevisiae)*	10574944	− 0.21	0.10	0.1347	tRNA processing/metabolic process/oxidation reduction
Gabra2	*Gamma-aminobutyric acid (GABA) A receptor, subunit alpha 2*	10530406	− 0.23	0.15	0.3174	Transport/ion transport/chloride transport/gamma-aminobutyric acid signaling pathway
Gfm2	*G elongation factor, mitochondrial 2*	10406795	− 0.21	0.08	0.0538	Translation
Gstp1	***Glutathione S-transferase, pi 1***	**10464583**	**− 0.26**	**0.08**	**0.0030**	**Glutathione metabolic process/metabolic process**
Hdhd3	*Haloacid dehalogenase-like hydrolase domain containing 3*	10513604	− 0.21	0.12	0.2494	Metabolic process
Hkdc1	***Hexokinase domain containing 1***	**10369567**	**− 0.21**	**0.07**	**0.0244**	**Glycolysis**
Hmgb1	*High-mobility group box 1*	10535894	− 0.25	0.11	0.0905	Eye development/positive regulation of protein amino acid phosphorylation/positive regulation of mesenchymal cell proliferation/positive regulation of specific transcription from RNA polymerase II promoter/lung development/positive regulation of cell migration/DNA geometric change/positive regulation of myeloid cell differentiation/positive regulation of glycogen catabolic process/positive regulation of mitotic cell cycle/induction of positive chemotaxis/response to glucocorticoid stimulus
Hsd17b7	*Hydroxysteroid (17-beta) dehydrogenase 7*	10359917	− 0.26	0.13	0.2044	Steroid biosynthetic process/cholesterol biosynthetic process/metabolic process/lipid biosynthetic process/oxidation reduction
Hyou1	***Hypoxia upregulated 1***	**10584712**	**− 0.23**	**0.08**	**0.0304**	**Response to stress**
Ifitm7	***Interferon-induced transmembrane protein 7***	**10437846**	**− 0.27**	**0.10**	**0.0184**	–
Igf2bp1	***Insulin-like growth factor 2 mRNA binding protein 1***	**10390211**	**− 0.21**	**0.08**	**0.0280**	**Regulation of translation**
Irx6	***Iroquois-related homeobox 6 (Drosophila)***	**10573916**	**− 0.22**	**0.08**	**0.0406**	**Regulation of transcription, DNA-dependent/biological process/regulation of transcription**
Katnal2	***Katanin p60 subunit A-like 2***	**10459804**	**− 0.25**	**0.09**	**0.0220**	–
Kif23	***Kinesin family member 23***	**10594251**	**− 0.21**	**0.08**	**0.0199**	–
Mapk11	***Mitogen-activated protein kinase 11***	**10431410**	**− 0.20**	**0.08**	**0.0411**	**Protein amino acid phosphorylation/protein kinase cascade**

Table 2 (continued)

Gene symbol	Gene title	Affymetrix transcript cluster ID	Average log2-fold	SEM log2-fold	*p* value	Biological process
Mfsd2	*Major facilitator superfamily domain containing 2A*	10516064	−0.24	0.10	0.0545	Transport
Mns1	***Meiosis-specific nuclear structural protein 1***	**10586907**	**−0.37**	**0.14**	**0.0314**	**Meiosis**
Mrps26	*Mitochondrial ribosomal protein S26*	10476189	−0.23	0.11	0.1551	–
Mtap1a	*Microtubule-associated protein 1 A*	10475314	−0.32	0.13	0.0605	Sensory perception of sound
Mthfd2	***Methylenetetrahydrofolate dehydrogenase (NAD+ dependent), methenyltetrahydrofolate cyclohydrolase***	**10545672**	**−0.23**	**0.08**	**0.0128**	**1-carbon compound metabolic process/folic acid and derivative biosynthetic process/oxidation reduction**
Mtx2	*Metaxin 2*	10472994	−0.26	0.12	0.1137	Transport/protein transport
Mvk	***Mevalonate kinase***	**10524555**	**−0.21**	**0.07**	**0.0041**	**Steroid biosynthetic process/cholesterol biosynthetic process/metabolic process/isoprenoid biosynthetic process/lipid biosynthetic process/sterol biosynthetic process/phosphorylation**
Myo9a	*Myosin IXa*	10585976	−0.22	0.10	0.1107	Signal transduction/intracellular signaling cascade
Ncl	*Nucleolin*	10356329	−0.20	0.20	0.5377	–
Nipa1	*Non-imprinted in Prader-Willi/Angelman syndrome 1 homolog (human)*	10563852	−0.24	0.13	0.2322	–
Nnt	***Nicotinamide nucleotide transhydrogenase***	**10412394**	**−0.30**	**0.11**	**0.0133**	**Metabolic process/proton transport/oxidation reduction**
Nr2f6	*Nuclear receptor subfamily 2, group F, member 6*	10579479	−0.21	0.10	0.1660	Transcription/regulation of transcription, DNA-dependent/entrainment of circadian clock by photoperiod/neuron development/detection of temperature stimulus involved in sensory perception of pain
Pdpn	*Podoplanin*	10518147	−0.22	0.09	0.0956	Cell morphogenesis/lymphangiogenesis/prostaglandin metabolic process/water transport/amino acid transport/cell motion/cell cycle/cell adhesion/signal transduction/multicellular organismal development/cell proliferation/regulation of cell shape/folic acid transport/cell-cell adhesion/lung development/positive regulation of cell migration/tube morphogenesis/alveolus development/positive regulation of cell motion
Pgf	*Placental growth factor*	10401607	−0.25	0.15	0.2666	Angiogenesis/ureteric bud branching/multicellular organismal development/cell proliferation/cell differentiation
Ppp1r1c	*Protein phosphatase 1, regulatory (inhibitor) subunit 1C*	10473180	−0.37	0.16	0.0798	Signal transduction
Pptc7	***PTC7 protein phosphatase homolog (S. cerevisiae)***	**10525374**	**−0.20**	**0.08**	**0.0398**	**–**
Prelp	*Proline arginine-rich end leucine-rich repeat*	10357870	−0.21	0.18	0.4658	Cell aging
Prkdc	***Protein kinase, DNA activated, catalytic polypeptide***	**10433797**	**−0.24**	**0.08**	**0.0138**	**Telomere maintenance/somitogenesis/B cell lineage commitment/pro-B cell differentiation/T cell lineage commitment/DNA repair/double-strand break repair/double-strand break repair via nonhomologous end joining/apoptosis/response to DNA damage stimulus/brain development/heart development/response to gamma radiation/peptidyl-serine phosphorylation/lymphocyte differentiation/protein destabilization/T cell differentiation in the thymus/immunoglobulin V(D)J recombination/T cell receptor V(D)J recombination/germ cell programmed cell death/positive regulation of apoptosis**
Ptges2	*Prostaglandin E synthase 2*	10471411	−0.22	0.09	0.0845	Prostaglandin biosynthetic process/fatty acid biosynthetic process/lipid biosynthetic process/regulation of transcription/cell redox homeostasis/secretion
Ptges3	***Prostaglandin E synthase 3 (cytosolic)***	**10367100**	**−0.24**	**0.09**	**0.0266**	**Prostaglandin biosynthetic process/fatty acid biosynthetic process/biological process/lipid biosynthetic process**
Rangrf	*RAN guanine nucleotide release factor*	10500683	−0.20	0.08	0.0511	Transport/nucleocytoplasmic transport/protein transport
Rcan2	*Regulator of calcineurin 2*	10445325	−0.20	0.11	0.2253	Calcium-mediated signaling
Rcvrn	*Recoverin*	10377235	−0.23	0.12	0.1813	Visual perception/phototransduction/response to stimulus/regulation of calcium ion transport
Rtn4ip1	*Reticulon 4 interacting protein 1*	10362904	−0.28	0.11	0.0704	Biological process/oxidation reduction

Table 2 (continued)

Gene symbol	Gene title	Affymetrix transcript cluster ID	Average log2-fold	SEM log2-fold	*p* value	Biological process
Scn2a1	***Sodium channel, voltage-gated, type II, alpha 1***	**10472378**	**−0.26**	**0.09**	**0.0018**	**Transport/ion transport/potassium ion transport/sodium ion transport/apoptosis/nervous system development**
Slc16a7	*Solute carrier family 16 (monocarboxylic acid transporters), member 7*	10372988	−0.22	0.12	0.1920	Transport/organic anion transport
Slc17a7	*Mus musculus solute carrier family 17 (sodium-dependent inorganic phosphate cotransporter), member 7 (Slc17a7), mRNA*	10552857	−0.23	0.16	0.3684	Transport/ion transport/sodium ion transport/neurotransmitter transport/sequestering of neurotransmitter/response to stimulus
Slc7a3	*Solute carrier family 7 (cationic amino acid transporter, y+ system), member 3*	10605986	−0.23	0.17	0.3875	Transport/amino acid transport/arginine transport/lysine transport
Snai2	***Snail homolog 2 (Drosophila)***	**10433776**	**−0.21**	**0.07**	**0.0102**	**Transcription/regulation of transcription, DNA-dependent/multicellular organismal development/response to radiation/response to radiation/regulation of survival gene product expression**
Snupn	*Snurportin 1*	10585601	−0.24	0.11	0.1435	Protein import into nucleus/transport/intracellular protein transport
Srp54b	*Signal recognition particle 54B*	10395739	−0.21	0.08	0.0502	–
Syne2	*Synaptic nuclear envelope 2*	10396608/10396606	−0.23	0.12	0.0638	–
Usp13	***Ubiquitin-specific peptidase 13 (isopeptidase T-3)***	**10491414**	**−0.21**	**0.07**	**0.0056**	**Modification-dependent protein catabolic process**
Zdhhc23	*Zinc finger, DHHC domain containing 23*	10439542	−0.21	0.11	0.2219	–
Zfp143	***Zinc finger protein 143***	**10556246**	**−0.21**	**0.07**	**0.0184**	**Transcription/regulation of transcription, DNA-dependent**
Upregulated genes						
Acsl3	*Acyl-CoA synthetase long-chain family member 3*	10347748	0.21	0.08	0.0600	Lipid metabolic process, fatty acid metabolic process/metabolic process
Adcy8	*Adenylate cyclase 8*	10429029	0.28	0.13	0.1395	cAMP biosynthetic process/intracellular signaling cascade/long-term memory/cyclic nucleotide biosynthetic process
Agtr1a	***Angiotensin II receptor, type 1a***	**10404376**	**0.24**	**0.08**	**0.0010**	**Blood vessel development/kidney development/regulation of systemic arterial blood pressure by circulatory renin-angiotensin/renin secretion into the bloodstream/renin-angiotensin regulation of aldosterone production/regulation of renal output by angiotensin/brain renin-angiotensin system/signal transduction/G protein-coupled receptor protein signaling pathway/drinking behavior/negative regulation of neuron apoptosis/positive regulation of blood pressure angiotensin II receptor, type 1a**
Ankrd37	*Ankyrin repeat domain 37*	10578515	0.23	0.12	0.2127	–
Anxa2	*Annexin A2*	10586744	0.32	0.17	0.2082	Angiogenesis/collagen fibril organization/fibrinolysis
Apln	***Apelin***	**10604375**	**0.22**	**0.09**	**0.0435**	**G protein-coupled receptor protein signaling pathway**
C1qa	*Complement component 1, q subcomponent, alpha polypeptide*	10517517	0.21	0.09	0.0779	Immune response/complement activation, classical pathway/innate immune response
C1qc	*Complement component 1, q subcomponent, C chain*	10517513	0.21	0.10	0.1168	Immune response/complement activation, classical pathway/innate immune response
Cabc1	*Chaperone, ABC1 activity of bc1 complex like (S. pombe)*	10360631	0.21	0.10	0.1768	–
Ccnt1	***Cyclin T1***	**10432180**	**0.20**	**0.08**	**0.0374**	**Transcription/regulation of transcription, DNA-dependent/protein amino acid phosphorylation/cell cycle/cell division**
Cdkn1b	*Cyclin-dependent kinase inhibitor 1B*	10542317	0.21	0.15	0.3801	Potassium ion transport/cell cycle/cell cycle arrest/sensory perception of sound/positive regulation of cell proliferation/negative regulation of cell proliferation/positive regulation of microtubule polymerization/negative regulation of cyclin-dependent protein kinase activity/inner ear development/negative regulation of epithelial cell proliferation/negative regulation of cell motion
Crybb3	*Crystallin, beta B3*	10532660	0.25	0.12	0.1694	–
D4Bwg0951e	***DNA segment, Chr 4, Brigham and Women's Genetics 0951 expressed***	**10505623**	**0.22**	**0.08**	**0.0369**	**–**
Efhd1	***EF hand domain containing 1***	**10348194**	**0.26**	**0.08**	**0.0010**	**Neuron projection development**

Table 2 (continued)

Gene symbol	Gene title	Affymetrix transcript cluster ID	Average log2-fold	SEM log2-fold	*p* value	Biological process
Efhd2	*EF hand domain containing 2*	10518069	0.23	0.14	0.2817	–
Egr1	*Early growth response 1*	10454782	0.24	0.13	0.2396	Negative regulation of transcription from RNA polymerase II promoter/transcription/regulation of transcription, DNA-dependent/T cell differentiation/response to protein stimulus
Eng	*Endoglin*	10471486	0.29	0.14	0.1522	Chronological cell aging/angiogenesis/patterning of blood vessels/vasculogenesis/heart looping/cell adhesion/heart development/regulation of transforming growth factor beta receptor signaling pathway/smooth muscle tissue development/artery morphogenesis/venous blood vessel morphogenesis
Epha2	*Eph receptor A5*	10509965	0.22	0.15	0.3525	Protein amino acid phosphorylation/transmembrane receptor protein tyrosine kinase signaling pathway/neuron differentiation/neuron differentiation/ephrin receptor signaling pathway
Fam55d	*Family with sequence similarity 55, member D*	10585068	0.25	0.17	0.3306	–
Fcgr3	*Fc receptor, IgG, low affinity III*	10360040	0.27	0.14	0.1953	Antibody-dependent cellular cytotoxicity/positive regulation of type IIa hypersensitivity/positive regulation of type III hypersensitivity/positive regulation of type I hypersensitivity/serotonin secretion/phagocytosis, recognition/phagocytosis, engulfment/cell surface receptor-linked signal transduction/neutrophil chemotaxis/positive regulation of tumor necrosis factor biosynthetic process/antigen processing and presentation of exogenous peptide antigen via MHC class I/mast cell activation/positive regulation of phagocytosis/regulation of immune response
Flt1	*FMS-like tyrosine kinase 1*	10535807	0.35	0.16	0.1294	Angiogenesis/patterning of blood vessels/protein amino acid phosphorylation/transmembrane receptor protein tyrosine kinase signaling pathway/multicellular organismal development/cell migration/cell differentiation/vascular endothelial growth factor receptor signaling pathway/vascular endothelial growth factor receptor signaling pathway
Gja1	*Gap junction protein, alpha 1*	10363173	0.29	0.14	0.1315	In utero embryonic development/neuron migration/heart looping/epithelial cell maturation/cell communication/cell-cell signaling/heart development/adult heart development/regulation of heart contraction/embryonic heart tube development/skeletal muscle regeneration/positive regulation of striated muscle development/blood vessel morphogenesis
Glcci1	*Glucocorticoid-induced transcript 1*	10536390	0.21	0.10	0.1349	–
Grid2	***Glutamate receptor, ionotropic, delta 2***	**10538732**	**0.22**	**0.08**	**0.0113**	**Transport/ion transport/synaptic transmission, glutamatergic/regulation of neuron apoptosis/regulation of neuron apoptosis/regulation of excitatory postsynaptic membrane potential/prepulse inhibition**
Gstm3	***Glutathione S-transferase, mu 3***	**10362511**	**0.25**	**0.09**	**0.0305**	**Metabolic process**
Igfbp3	***Insulin-like growth factor binding protein 3***	**10384223**	**0.21**	**0.08**	**0.0399**	**Regulation of cell growth/osteoblast differentiation/negative regulation of protein amino acid phosphorylation/protein amino acid phosphorylation**
Igfbp5	*Insulin-like growth factor binding protein 5*	10355500	0.24	0.11	0.1142	Regulation of cell growth/osteoblast differentiation
Irs2	*Insulin receptor substrate 2*	10576971	0.24	0.14	0.2481	Positive regulation of mesenchymal cell proliferation/signal transduction/brain development/cell proliferation/insulin receptor signaling pathway/positive regulation of cell migration/mammary gland development
Jag1	***Jagged 1***	**10488060**	**0.21**	**0.07**	**0.0059**	**Morphogenesis of an epithelial sheet/cell communication/Notch signaling pathway/multicellular organismal development/organ morphogenesis/auditory receptor cell differentiation/negative regulation of cell differentiation/positive regulation of myeloid cell differentiation/positive regulation of Notch signaling pathway/inner ear development**
Klf13	*Kruppel-like factor 13*	10564290	0.22	0.10	0.1428	Transcription/regulation of transcription, DNA-dependent/transcription from RNA polymerase II promoter/positive regulation of transcription from RNA polymerase II promoter

Table 2 (continued)

Gene symbol	Gene title	Affymetrix transcript cluster ID	Average log2-fold	SEM log2-fold	*p* value	Biological process
Klf15	*Kruppel-like factor 15*	10540028	0.22	0.09	0.0542	Transcription/regulation of transcription, DNA-dependent/glucose transport/positive regulation of transcription, DNA-dependent
Krtap10-10	*Keratin-associated protein 10-10*	10364326	0.30	0.14	0.1454	–
Lphn2	*Latrophilin 2*	10502772	0.24	0.17	0.3625	Signal transduction/cell surface receptor-linked signal transduction/G protein-coupled receptor protein signaling pathway/neuropeptide signaling pathway
Luzp2	***Leucine zipper protein 2***	**10553537**	**0.23**	**0.08**	**0.0188**	–
Ly86	*Lymphocyte antigen 86*	10404606	0.20	0.13	0.3259	Inflammatory response/immune response
Maff	*V-maf musculoaponeurotic fibro-sarcoma oncogene family, protein F (avian)*	10425283	0.31	0.15	0.1438	In utero embryonic development/transcription/regulation of transcription, DNA-dependent/regulation of epidermal cell differentiation
Nkx2–9	***NK2 transcription factor related, locus 9 (Drosophila)***	**10400479**	**0.28**	**0.10**	**0.0266**	**Regulation of transcription, DNA-dependent/multicellular organismal development/axonogenesis/respiratory tube development/lung development/regulation of transcription/negative regulation of epithelial cell proliferation**
Optc	*Opticin*	10357858	0.35	0.18	0.1983	–
Pcmtd2	*Protein-L-iso-aspartate (D-aspartate) O-methyl-transferase domain containing 2*	10479726	0.23	0.10	0.1147	Protein modification process
Pdlim3	*PDZ and LIM domain 3*	10571601	0.28	0.12	0.1173	Actin filament organization/heart development/skeletal muscle tissue development
Pfkfb3	*6-phospho-fructo-2-kinase/fructose-2,6-biphos-phatase 3*	10480035	0.31	0.20	0.3273	–
Pnpla2	*Patatin-like phospho-lipase domain containing 2*	10558921	0.22	0.13	0.2734	Lipid metabolic process/lipid catabolic process/triglyceride catabolic process
Ptgds	*Prostaglandin D2 synthase (brain)*	10480734	0.22	0.11	0.2054	Prostaglandin biosynthetic process/lipid metabolic process/fatty acid biosynthetic process/transport/lipid biosynthetic process/regulation of circadian sleep/wake cycle, sleep
Rbm25	***RNA-binding motif protein 25***	**10397068/10397081**	**0.23**	**0.07**	**0.0001**	**mRNA processing**
Rmnd5a	*Required for meiotic nuclear division 5 homolog A (S. cerevisiae)*	10545298	0.21	0.08	0.0753	–
Rmrp	*RNA component of mitochondrial RNAase P*	10512487	0.26	0.12	0.1434	–
Rnasel	*Ribonuclease L (2',5'-oligoisoadenylate synthetase-dependent)*	10350742	0.21	0.09	0.0619	mRNA processing/protein amino acid phosphorylation
Rnu2	*U2 small nuclear RNA*	10603736	0.24	0.14	0.2744	–
Rpl13	*Ribosomal protein L13*	10576216	0.27	0.11	0.0615	Translation
Rpl7	***Ribosomal protein L7***	**10353265/10375461**	**0.21**	**0.07**	**0.0092**	**Translation**
Rprl2	*Ribonuclease P RNA-like 2*	10491058	0.20	0.12	0.2780	–
Rras	***Harvey rat sarcoma oncogene, subgroup R***	**10552824**	**0.22**	**0.08**	**0.0359**	**Small GTPase-mediated signal transduction/negative regulation of cell migration**
Runx2	***Runt-related transcription factor 2***	**10451061**	**0.23**	**0.07**	**0.0015**	**Skeletal system development/osteoblast differentiation/endochondral ossification/osteoblast fate commitment/chondrocyte differentiation/chondrocyte development/transcription/regulation of transcription, DNA-dependent/positive regulation of cell proliferation/regulation of ossification/positive regulation of chondrocyte differentiation/regulation of fibroblast growth factor receptor signaling pathway/odontogenesis of dentine-containing tooth/regulation of odontogenesis of dentine-containing tooth/positive regulation of osteoblast differentiation/negative regulation of smoothened signaling pathway/positive regulation of transcription from RNA polymerase II promoter**
Sat1	*Spermidine/spermine N1-acetyl transferase 1*	10607467	0.24	0.09	0.0522	Metabolic process/regulation of cell proliferation/spermine catabolic process
Sepp1	*Selenoprotein P, plasma, 1*	10422598	0.24	0.10	0.0738	Selenium metabolic process/selenium metabolic process/brain development/locomotory behavior/post-embryonic development/sexual reproduction/growth
Si	*Silver*	10367379	0.21	0.18	0.4724	Melanin biosynthetic process from tyrosine/melanin biosynthetic process
Slc13a4		**10543921**	**0.28**	**0.11**	**0.0453**	–

Table 2 (continued)

Gene symbol	Gene title	Affymetrix transcript cluster ID	Average log2-fold	SEM log2-fold	*p* value	Biological process
	Solute carrier family 13 (sodium/sulfate symporter, member 4)					
Slc38a5	*Solute carrier family 38, member 5*	10598507	0.22	0.12	0.1979	–
Slc38a9	*Solute carrier family 38, member 9*	10407192	0.21	0.09	0.1102	Transport/ion transport/sodium ion transport/amino acid transport
Slc44a5	*Solute carrier family 44, member 5*	10496975	0.21	0.10	0.1152	–
Snhg1	*Small nucleolar RNA host gene (non-protein coding) 1*	10461156	0.25	0.12	0.1409	–
Snora34	*Small nucleolar RNA, H/ACA box 34*	10432176	0.28	0.16	0.2354	–
Snord115	*Small nucleolar RNA, C/D Box 115 cluster*	10564011	0.31	0.14	0.1167	–
Snord35a	*Small nucleolar RNA, C/D box 35A*	10563108	0.25	0.10	0.0509	–
Snord49b	*Small nucleolar RNA, C/D box 49B*	10376885	0.24	0.11	0.1407	–
Sox9	*SRY-box containing gene 9*	10382328	0.22	0.12	0.2397	Cartilage condensation/cell fate specification/epithelial to mesenchymal transition/hair follicle development/transcription/regulation of transcription, DNA-dependent/heart development/male gonad development/neural crest cell development/male germ-line sex determination/cell differentiation/male sex determination/negative regulation of bone mineralization/negative regulation of chondrocyte differentiation/regulation of cell proliferation/regulation of apoptosis/cell fate commitment/negative regulation of transcription, DNA-dependent/positive regulation of transcription from RNA polymerase II promoter/positive regulation of transcription from RNA polymerase II promoter/cartilage development/endochondral bone morphogenesis
Stab1	*Stabilin 1*	10418506	0.25	0.11	0.1117	Inflammatory response/cell adhesion
Stc1	*Stanniocalcin 1*	10416181	0.26	0.11	0.0815	Cellular calcium ion homeostasis/cellular monovalent inorganic anion homeostasis
Timp3	***Tissue inhibitor of metalloproteinase 3***	**10365482**	**0.20**	**0.07**	**0.0213**	**Transmembrane receptor protein tyrosine kinase signaling pathway**
Trf	*Transferrin*	10596148	0.23	0.12	0.1718	Transport/ion transport/iron ion transport/cellular iron ion homeostasis
Usp2	*Ubiquitin-specific peptidase 2*	10584634	0.22	0.14	0.3131	Ubiquitin-dependent protein catabolic process/modification-dependent protein catabolic process
Vwf	*Von Willebrand factor homolog*	10541910	0.20	0.10	0.1577	Liver development/placenta development/cell adhesion/blood coagulation/hemostasis/hemostasis/platelet activation/cell-substrate adhesion
Wfdc1	***WAP 4-disulfide core domain 1***	**10575917**	**0.34**	**0.12**	**0.0273**	**–**
Zfp322a	*Zinc finger protein 322A*	10408162	0.21	0.11	0.2154	Transcription/regulation of transcription, DNA-dependent
Zfp69	*Zinc finger protein 69*	10515986	0.37	0.25	0.3552	Transcription
Zfp711	***Zinc finger protein 711***	**10601492**	**0.23**	**0.08**	**0.0163**	**–**

Dysregulated genes with a p value < 0.05 are shown in bold

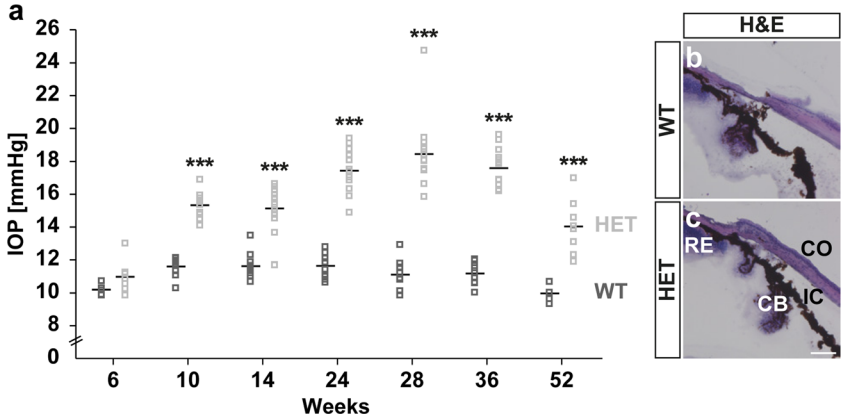

Fig. 1 Intraocular pressure (IOP) elevation in *Meg2* HET mice. **a** IOP of both eyes was measured in *Meg2* HET and control WT littermates at 6 weeks, 10 weeks, 14 weeks, 24 weeks, 28 weeks, 36 weeks, and 52 weeks ($n = 6$–13). *Meg2* HET mice developed IOP elevation at 10 weeks. **b**, **c** Morphopathological analyses of the iridocorneal angle. H&E staining revealed an open angle in WT and *Meg2* HET mice ($n = 5$). ***$p < 0.001$. Per animal, 10 measurements per eye were averaged. The mean value per animal is shown as a box, while the mean value of all animals in the compared groups is shown as a line per point in time. Scale bar = 100 μm. CB ciliary body, CO cornea, H&E hematoxylin-eosin, IC iridocorneal angle, RE retina

0.30 mmHg) and HET (10.99 ± 1.02 mmHg; $p = 0.07$) animals. Measurements at 10 weeks revealed a significant IOP elevation in HET mice (WT, 11.61 ± 0.55 mmHg; HET, 15.33 ± 0.72 mmHg; $p < 0.001$). Also, at 14 weeks, a significant IOP elevation was evident (WT, 11.65 ± 0.79 mmHg; HET, 15.14 ± 1.33 mmHg; $p < 0.001$). Subsequently, at 24 weeks, IOP of HET mice (17.44 ± 1.30 mmHg) further increased, while WT animals (11.65 ± 0.71 mmHg; $p < 0.001$) maintained a steady mean IOP. At 28 weeks, IOP elevation peaked in HET mice (WT, 11.12 ± 0.84 mmHg; HET, 18.43 ± 2.17 mmHg; $p < 0.001$). At 36 weeks, we still measured a significantly elevated IOP in HET (17.60 ± 1.17 mmHg) compared to WT (11.19 ± 0.61 mmHg; $p < 0.001$) mice. Even though a slight decline of IOP values was observable in both genotypes at 1 year, IOP was significantly increased in HET mice (WT, 9.98 ± 0.46 mmHg; HET, 14.03 ± 1.67 mmHg; $p = 0.001$).

Morphopathological analyses of the iridocorneal angle via H&E staining revealed an open angle in WT as well as in adolescent HET mice (Fig. 1b, c).

Since rebound tonometry measurements can be affected by the corneal thickness, we next explored the CCT in WT and *Meg2* HET mice. However, measurements of H&E-stained eye sections revealed a comparable CCT in WT (122.69 ± 5.24 μm) and HET (113.75 ± 4.99 μm; $p = 0.94$; Figure S2) mice.

Heterozygous Loss of *Meg2* Causes Optic Nerve Degeneration and RGC Loss

Elevated IOP leads to a mechanical compression of the optic nerve head, which is expected to be the main reason for progressive optic nerve degeneration and RGC loss in high-pressure glaucoma. To assess axonal integrity and ultrastructural alterations, TEM was performed on optic nerve sections (Fig. 2a–d). In agreement with our previous findings, damage in the axonal ultrastructure was observed in optic nerves of HET mice at 1 year. In comparison to the WT, optic nerves of HET mice exhibited shrunken axons and vacuoles between the myelin sheath and axolemma. Some HET axons displayed thin and loosely packed myelin as well as myelin intrusions or extrusions, and single myelin sheaths lacked a central axon. Since IOP elevation peaked at around 28 weeks in HET mice, we conducted further analyses at this point in time. Compared to the WT (42.84 ± 11.76 area [%]/image), optic nerve axons of HET animals (18.52 ± 13.51 area [%]/image; $p = 0.035$) displayed significantly less NF-200 immunoreactivity as revealed by a reduced staining area, further confirming an impaired axonal density and integrity (Fig. 2e–g).

A hallmark of high-pressure glaucoma is the progressive loss of RGCs upon IOP elevation. To analyze RGCs in HET and WT mice, retinal sections were immunohistochemically stained using an antibody against Brn3a [40, 41] (Fig. 2h, i). Overall, a normal distribution and arrangement of $Brn3a^+$ RGCs was detected in WT retinae. In contrast, HET mice exhibited an obvious loss of $Brn3a^+$ RGCs. To investigate the impact of IOP elevation on RGCs in more detail, we analyzed retinal flat-mounts of HET and WT littermates at 28 weeks (Fig. 2j, k). Quantification of $Brn3a^+$ cells revealed a significant loss of RGCs in HET (1173.50 ± 77.35 cells/mm^2) compared to WT (1951.42 ± 27.91 cells/mm^2; $p < 0.001$; Fig. 2l) retinae. Analyses after chronic IOP elevation at > 1 year of age revealed a further RGC loss in HET (1105.16 ± 30.91 cells/mm^2) compared to WT (2073.69 ± 39.91 cells/mm^2; $p < 0.001$; Figure S3c) mice. In contrast, at 6 weeks, HET (1922.75 ± 46.00 cells/mm^2) and WT (2004.39 ± 45.00 cells/mm^2; $p = 0.274$; Figure S3a) mice still exhibited

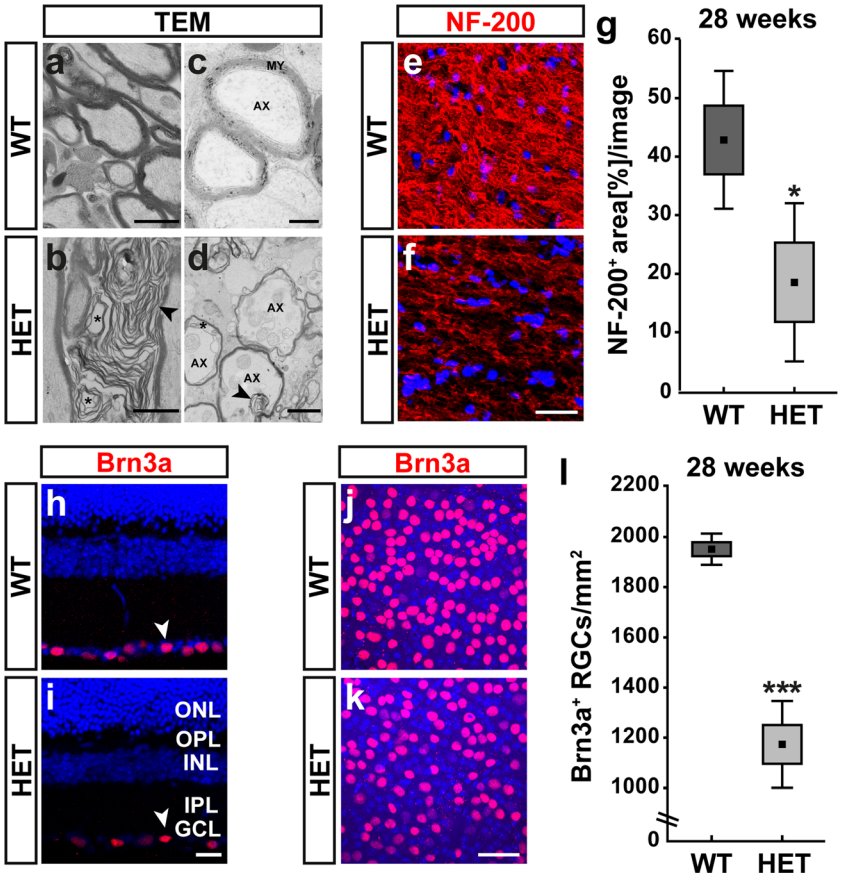

Fig. 2 Optic nerve damage and severe RGC loss in *Meg2* HET mice. **a**–**d** Ultrastructural electron microscopic analyses revealed massive optic nerve damage at 1 year ($n = 3$). In comparison to the WT, optic nerves of HET animals exhibited shrunken axons and several vacuoles were found between the myelin sheath and axolemma. Axons displayed thin, loosely packed myelin or myelin intrusions (arrowheads). Some axons showed a lack of a central axon (asterisks). **e**, **f** Representative photographs of NF-200 (red)-stained longitudinal optic nerve sections demonstrated impaired structural integrity in HET mice at 28 weeks, indicating severe optic nerve degeneration. **g** Quantification offered significantly reduced NF-200 immunostaining in HET mice ($n = 5$). **h**–**k** Representative photographs of Brn3a$^+$ RGCs (red) in retinal sections and flat-mounts of *Meg2* HET and WT mice at 28 weeks. Arrows in **h**, **i** point to Brn3a$^+$ cells in the GCL. **l** As noted by Brn3a$^+$ cell counts in retinal flat-mounts, HET mice exhibited a significant loss of RGCs ($n = 5$). Nuclei were stained with TO-PRO-3 (blue). $^*p < 0.05$, $^{***}p < 0.001$. Values in **g** and **l** are shown as mean ± SEM ± SD. Scale bars = 1 μm in **a**–**d**, 50 μm in **f** and **k**, and 20 μm in **i**. AX axolemma, GCL ganglion cell layer, INL inner nuclear layer, IPL inner plexiform layer, MY myelin, ONL outer nuclear layer, OPL outer plexiform layer

comparable numbers of Brn3a$^+$ RGCs. Also, at 10 weeks, the number of Brn3a$^+$ RGCs was comparable in both genotypes (WT, 2022.93 ± 133.55 cells/mm^2; HET, 1948.83 ± 87.68 cells/mm^2; $p = 0.667$; Figure S3b), which indicates a loss of RGCs at later points in time.

Interestingly, we observed an irregular and smaller nuclear morphology of Brn3a$^+$ RGCs in HET retinae at late adolescence. Brn3a$^+$ nuclei of WT mice showed a regular, round, or oval morphology. To analyze this morphology in more detail, we measured the circumference and area of Brn3a$^+$ nuclei at 28 weeks. Indeed, quantification of the circumference of Brn3a$^+$ nuclei revealed a significantly reduced nuclei size in HET (32.87 ± 0.36 μm) compared to WT retinae (37.42 ± 0.73 μm; $p < 0.001$; Figure S4a). Additionally, area analyses of Brn3a$^+$ nuclei showed severe nuclei shrinkage in the HET group (WT, 112.70 ± 4.31 μm^2; HET, 87.04 ± 1.99 μm^2; $p < 0.001$; Figure S4b).

Elevated Macrogliosis in *Meg2* HET Retinae and Optic Nerves

Retinal neurodegeneration is often accompanied by gliosis [42–44]. To explore retinal macroglia in HET mice, we analyzed astrocyte and Müller glia populations at various points in time (Fig. 3 and Figure S5b). At 28 weeks, immunohistochemistry on retinal flat-mounts (Fig. 3a, b) and sections (Fig. 3f, g) revealed reactive macrogliosis in HET retinae, as verified by a larger GFAP staining area. HET astrocytes displayed an apparent activated morphology, by means of thicker and more intensely stained processes compared to WT astrocytes (Fig. 3c, d; zoom). Evaluation of GFAP immunoreactivity showed a significant area increase in flat-mounts of HET (27.12 ± 3.79 area [%]/image) compared to WT (13.56 ± 4.67 area [%]/image; $p = 0.017$; Fig. 3e) retinae at 28 weeks. Additionally, analyses of retinal sections

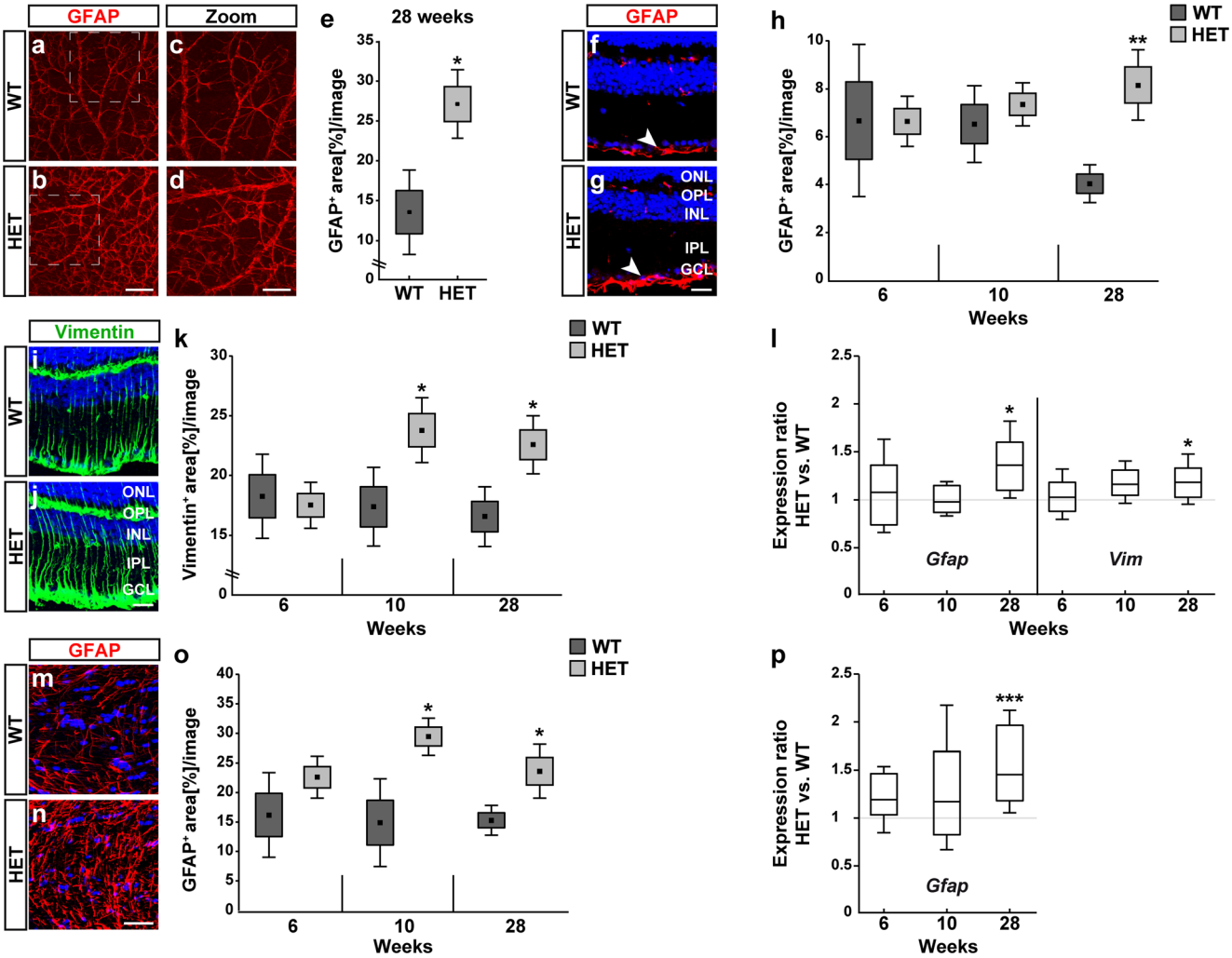

Fig. 3 Increased macrogliosis in the *Meg2* HET retina and optic nerve. **a**, **b** Representative photographs of GFAP$^+$ astroglia (red) in flat-mount retinae of WT and HET mice at 28 weeks. **c**, **d** Astroglial morphology is also shown in a higher magnification (zoom). **e** Significant increase of the GFAP staining area was observed in HET compared to WT retinae ($n = 3$). **f**, **g** GFAP immunolabeling (red, arrowheads) in retinal sections of WT and HET mice at 28 weeks. **h** At this point in time, a significant increase of the GFAP staining area was observed in HET retinae ($n = 4$). In contrast, a comparable GFAP$^+$ area was found in the retinae of both genotypes at 6 weeks and 10 weeks ($n = 3$–4). **i**, **j** Exemplary photographs of vimentin$^+$ Müller glia (green) in retinal sections of WT and HET mice at 28 weeks. **k** Analyses of the vimentin staining area revealed a significant increase in the HET retinae at 28 weeks and 10 weeks, but not at 6 weeks ($n = 3$–4). **l** Analyses of the relative *Gfap* and *Vim* mRNA expression by RT-qPCR ($n = 4$). In comparison to the WT, a significant upregulation was found for *Gfap* and *Vim* expression levels in HET retinae at 28 weeks, but not at 6 weeks or 10 weeks. **m**, **n** Representative photographs of GFAP$^+$ astroglia (red) in optic nerve sections of WT and HET mice at 28 weeks. **o** Quantification revealed a significant increase in the GFAP staining area of HET compared to WT mice at 28 weeks and 10 weeks, but not at 6 weeks ($n = 3$–4). **p** As shown by RT-qPCR, *Gfap* expression levels were significantly increased in HET compared to WT optic nerves at 28 weeks. No regulation of *Gfap* was observed at 6 weeks and 10 weeks ($n = 3$). Nuclei were stained with TO-PRO-3 (blue). $^*p < 0.05$, $^{**}p < 0.01$, $^{***}p < 0.001$. Values in **e**, **h**, **k**, and **o** are shown as mean ± SEM and SD. Values in **l** and **p** are shown as median ± quartile ± minimum (min)/maximum (max). Scale bars = 100 μm in **b**, 50 μm in **d** and **n**, and 20 μm in **g** and **j**. GCL ganglion cell layer, INL inner nuclear layer, IPL inner plexiform layer, ONL outer nuclear layer, OPL outer plexiform layer

showed a significant increase of GFAP staining area in HET mice (WT, 4.03 ± 0.81 area [%]/image; HET, 8.16 ± 1.50 area [%]/image; $p = 0.003$; Fig. 3h). Also, at > 1 year of age, following chronic IOP elevation (Figure S5a), a significantly larger GFAP$^+$ staining area was observed in HET flat-mount retinae (25.57 ± 1.19 area [%]/image) compared to the WT (21.55 ± 1.08 area [%]/image; $p = 0.036$; Figure S5b). Contrary, we observed a comparable GFAP staining area at 10 weeks (WT, 6.52 ± 1.42 area [%]/image; HET, 7.35 ± 0.80 area [%]/image; $p = 0.429$) and 6 weeks (WT, 6.67 ± 3.25 area [%]/image; HET, 6.63 ± 1.07 area [%]/image; $p = 0.986$) in both genotypes (Fig. 3h). We also analyzed vimentin staining of Müller glia in both groups (Fig. 3i, j). Our analyses revealed a significant increase in the vimentin staining area in HET animals at 28 weeks (WT, 16.57 ± 2.55 area [%]/image; HET, 22.57 ± 2.48 area [%]/image; $p = 0.015$) and 10 weeks (WT, 18.18 ± 2.91 area [%]/image; HET, 24.57 ± 2.40 area [%]/image; $p = 0.042$;

Fig. 3k). A comparable vimentin area was observed in retinae of both genotypes at 6 weeks (WT, 18.27 ± 3.58 area [%]/image; HET, 17.53 ± 1.96 area [%]/image; $p = 0.730$; Fig. 3k). RT-qPCR analyses verified a significant upregulation of *Gfap* (1.36-fold; $p = 0.035$) and *Vim* (1.18-fold; $p = 0.025$) expression in HET retinae at 28 weeks, while no differences were found at earlier points in time ($p > 0.05$; Fig. 3l; Table S6). Moreover, we analyzed the GFAP staining area of astrocytes in optic nerve sections at 6 weeks, 10 weeks, and 28 weeks (Fig. 3m, n). Our quantification revealed a significantly increased GFAP staining area in HET compared to WT mice at 28 weeks (WT, 15.29 ± 2.57 area [%]/image; HET, 23.61 ± 4.66 area [%]/image; p = 0.02) and 10 weeks (WT, 15.18 ± 6.49 area [%]/image; HET, 29.55 ± 2.73 area [%]/image; $p = 0.024$; Fig. 3o). No differences were observed at 6 weeks (WT, 16.47 ± 7.23 area [%]/image; HET, 22.79 ± 3.58 area [%]/image; $p = 0.169$; Fig. 3o). RT-qPCR analyses showed a significant elevated *Gfap* expression in optic nerves of HET mice (1.44-fold; $p < 0.001$) at 28 weeks, while comparable levels were observed at 10 weeks (1.16-fold; $p = 0.503$) and 6 weeks (1.19-fold; $p = 0.125$; Fig. 3p; Table S5).

Meg2 HET Mice Exhibit Reactive Microglia Response

In the process of retinal neurodegeneration, microglial cells can undergo activation [45–47]. Thus, we assessed microglia using an antibody against Iba1 in retinae and optic nerves of both groups at various times. Compared to the WT, microglia in HET animals showed a reactive, amoeboid morphology. At 28 weeks, higher Iba1$^+$ cell numbers were observed in retinal flat-mounts (Fig. 4a–d) and sections (Fig. 4f–k) of HET compared to WT mice. Counts revealed 169.69 ± 10.40 Iba1$^+$ cells/mm^2 in WT flat-mounts, while a significantly increased number of 240.70 ± 12.03 cells/mm^2 were noted in HET flat-mounts ($p = 0.011$; Fig. 4e). Evaluation of retinal sections revealed a higher number of microglia in the ganglion cell layer (GCL) and inner plexiform layer (IPL) of HET retinae (2.64 ± 0.85 cells/mm) compared to WT retinae (1.62 ± 0.40 cells/mm; $p = 0.047$; Fig. 4l). Also, the number of iNOS$^+$ + Iba1$^+$ reactive microglia was elevated in retinal sections of HET mice (WT, 0.81 ± 0.33 cells/mm; HET, 1.50 ± 0.52 cells/mm; $p = 0.046$; Fig. 4m). In line with an increased infiltration of reactive microglia in HET retinae, RT-qPCR analyses verified elevated *Nos2* mRNA expression levels at 28 weeks

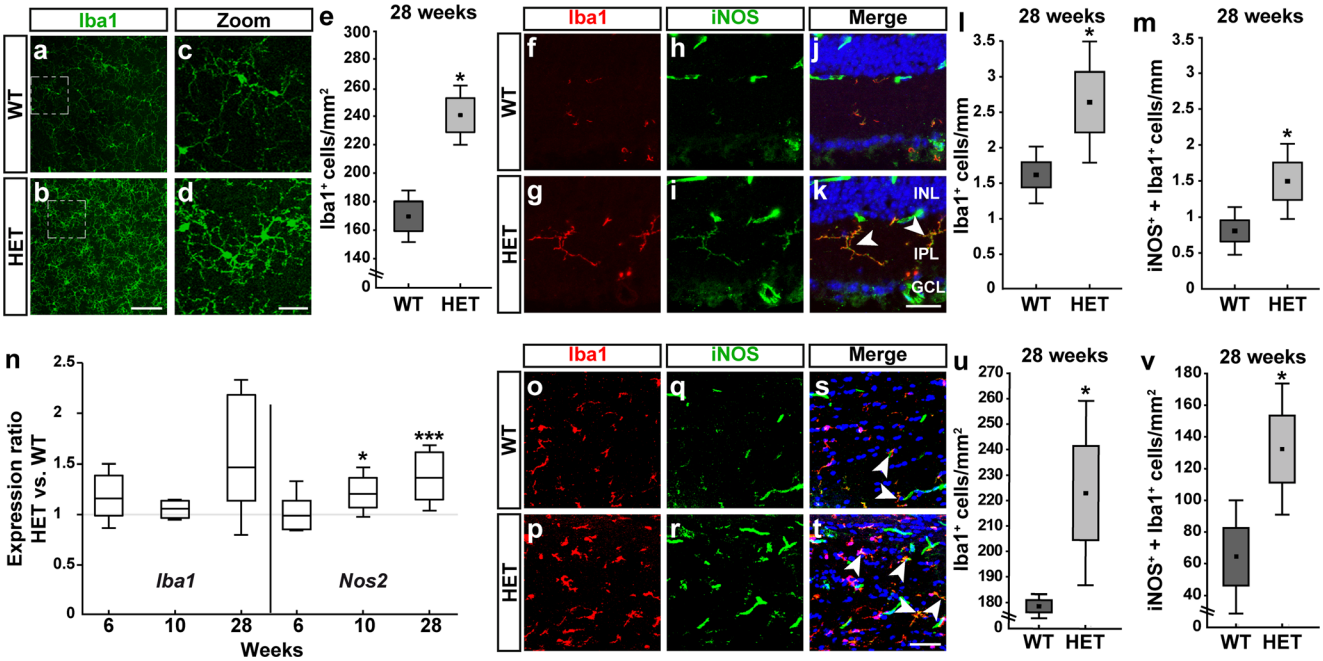

Fig. 4 More microglia in the retina and optic nerve of *Meg2* HET mice. **a**–**d** Representative photographs of Iba1$^+$ microglia (green) in flat-mount retinae of WT and HET mice at 28 weeks. **c**, **d** Microglial morphology is shown in a higher magnification (zoom). **e** A significant increase in the number of Iba1$^+$ microglia was noted in HET compared to WT retinae ($n = 3$). **f**–**k** iNOS and Iba1 double immunostaining (green, red) in retinal sections of WT and HET mice at 28 weeks showed co-localization of both markers (**k**; arrowheads). The number of Iba1$^+$ microglia (**l**) as well as iNOS$^+$ + Iba1$^+$ reactive (**m**) ones was significantly increased in the GCL/IPL of HET retinae ($n = 4$–5). **n** Analyses of the relative *Iba1* and *Nos2* mRNA expression using RT-qPCR ($n = 3$–4). Compared to WT mice, a significant upregulation of *Nos2* expression levels was found in HET retinae at 28 weeks and 10 weeks. No significant changes were observed regarding the *Iba1* expression level at these points in time. At 6 weeks, comparable levels of *Iba1* and *Nos2* mRNA expression levels were found. **o**–**t** Representative photographs show iNOS$^+$ + Iba1$^+$ reactive microglia (arrowheads) in optic nerve sections of WT and HET mice at 28 weeks. Quantification revealed a significantly increased number of Iba1$^+$ (**u**) as well as iNOS$^+$ + Iba1$^+$ microglia (**v**) in HET compared to WT mice ($n = 4$–5). Nuclei were stained with TO-PRO-3 (blue). *$p < 0.05$, ***$p < 0.001$. Values in **e**, **l**, **m**, **u**, **v** are shown as mean ± SEM and SD. Values in **n** are shown as median ± quartile ± min/max. Scale bars = 100 μm in **b**, 50 μm in **d** and **t**, and 20 μm in **k**. GCL ganglion cell layer, INL inner nuclear layer, IPL inner plexiform layer

(1.35-fold; $p < 0.001$) and 10 weeks (1.21-fold; $p = 0.042$; Fig. 4n). However, no significant change in the *Iba1* expression level was found at all points in time ($p > 0.05$; Fig. 4n; Table S5). To analyze microgliosis after chronic, long-term IOP elevation (Figure S5a), we performed Iba1 immunostaining in retinal flat-mounts at a late point in time, namely at > 1 year of age (Figure S5c). Here, our analyses still revealed a significantly higher number of $Iba1^+$ microglia in the HET retinae (WT, 147.95 ± 12.50 $Iba1^+$ cells/mm^2; HET, 186.12 ± 9.65 $Iba1^+$ cells/mm^2; $p = 0.042$).

Additionally, we analyzed the number and reactivity of microglia in optic nerve sections at 28 weeks (Fig. 4o–t). Evaluation revealed a significantly increased number of $Iba1^+$ microglia in HET animals (WT, 179.30 ± 5.88 cells/mm^2; HET, 223.31 ± 40.31 cells/mm^2; $p = 0.044$; Fig. 4u). Also, $iNOS^+$ + $Iba1^+$ microglia counts were higher in the HET (132.35 ± 42.22 cells/mm^2) compared to the WT optic nerves (64.34 ± 40.72 cells/mm^2; $p = 0.044$; Fig. 4v). However, RT-qPCR showed comparable *Iba1* and *Nos2* mRNA expression levels in optic nerves of both groups at 6 weeks, 10 weeks, and 28 weeks ($p > 0.05$; Table S5).

Classical Complement Activation in *Meg2* HET Mice

Complement components were reported to be elevated in human and in various experimental glaucoma animal models [9, 48–53]. In addition, complement activation in the retina and optic nerve head represents one of the earliest signaling responses to IOP elevation [53]. In the present study, a dysregulation of complement components was revealed in KO retinae via microarray analyses. Due to these overall reports and our observations, we closely analyzed complement activation in the retina and optic nerve of HET mice at different points in time. As schematically illustrated, we specifically concentrated on complement components associated with the classical, alternative, and lectin pathway (Fig. 5a). At the end of these pathways, MAC is formed, which results in lysis of the target cell. This common final pathway was also analyzed. Analyses of *C1q* mRNA levels via RT-qPCR revealed a significant downregulation of *C1qa* (0.60-fold; $p = 0.017$), *C1qb* (0.48-fold; $p < 0.001$), and *C1qc* (0.46-fold; $p < 0.001$) expression in HET retinae at 28 weeks (Fig. 5b; Table S5). At 10 weeks, an early and significant upregulation of *C1qa* (1.96-fold; $p < 0.001$) and *C1qc* (1.38-fold; $p < 0.001$) expression was found, while *C1qb* levels were comparable in WT and HET retinae (1.02-fold; $p = 0.844$). Expression analyses at 6 weeks revealed a comparable *C1qa* (0.95-fold; $p = 0.854$), *C1qb* (1.05-fold; $p = 0.674$), and *C1qc* (0.93-fold; $p = 0.641$) mRNA level. This indicates an early IOP-dependent activation of the classical complement pathway in HET retinae at 10 weeks. Expression of the alternative pathway components *Cfb* and *C3* was comparable in both groups at all points in time ($p > 0.05$; Fig. 5c; Table S5). Components of the lectin pathway, namely *Masp2* and *C4*, showed no alteration ($p > 0.05$; Fig. 5d; Table S5). A lower *Mbl* expression level was observed at 10 weeks (0.82-fold; $p = 0.035$), whereas an increased *C2* level was verified at 28 weeks (1.50-fold; $p = 0.029$). The *C5* expression level was significantly increased in HET retinae at 28 weeks (1.28-fold; $p = 0.043$) as well as at 10 weeks (1.60-fold; $p = 0.034$), but not at 6 weeks (1.18-fold; $p = 0.167$; Fig. 5e; Table S4). To evaluate complement activation on protein level, we analyzed MAC immunoreactivity. MAC deposition in glaucomatous RGCs was reported in human eyes as well as in experimental glaucoma models [49, 54, 55]. An increased number of MAC^+ deposits were found in retinal and optic nerve sections of WT and HET mice (Fig. 5f, g, i, j). Analyses verified significantly elevated numbers of MAC^+ cells in the GCL of HET retinae (WT, 6.96 ± 1.24 mm; HET, 9.35 ± 0.60 mm; $p = 0.005$; Fig. 5h) at 28 weeks. The same was noted in optic nerves (WT, 37.76 ± 6.08 mm^2/area; HET, 60.28 ± 13.00 mm^2/area; $p = 0.008$; Fig. 5k). No change in the number of MAC^+ cells was observed in retinae and optic nerves of both genotypes at 10 weeks ($p > 0.05$; data not shown).

Latanoprost Effectively Lowers IOP, Protects RGCs, and Reduces Microglial Invasion in *Meg2* HET Mice

Next, we tested the potential IOP-lowering effect of the prostaglandin analogue latanoprost (LT) in HET mice (Fig. 6a, b; Table S6). At 7 weeks, 8 weeks, and 9 weeks, a comparable IOP was detected in WT and HET mice ($p > 0.05$). As shown before, at 10 weeks, a significant IOP elevation was monitored in HET animals (15.31 ± 1.40 mmHg) compared to WT mice (13.15 ± 1.08 mmHg; $p = 0.008$). At 11 weeks, following daily LT administration starting at 10 weeks, treated HET mice (12.66 ± 1.03 mmHg) showed significantly reduced IOP values compared to non-treated HET mice (16.72 ± 3.78 mmHg; $p < 0.001$). Indeed, IOP measurements revealed that WT, LT-treated WT, and LT-treated HET mice exhibited a comparable IOP ($p = 1.0$). IOP measurements, conducted until 13 weeks, verified the IOP-lowering effect of LT in HET mice ($p < 0.001$; Table S6). In the next step, we addressed the question whether the IOP-lowering effect in HET mice correlates with RGC protection. Accordingly, $Brn3a^+$ cells were analyzed in retinal flat-mounts (Fig. 6c–j). We quantified the total number of $Brn3a^+$ RGCs (Fig. 6k) as well as the number of $Brn3a^+$ RGCs within the central (Fig. 6l) and peripheral (Fig. 6m) parts of the retina, following LT treatment up to 14 weeks. A significant reduction in the total number of RGCs was observed in retinae of non-treated HET animals (1260.55 ± 74.77 cells/mm^2) in comparison to non-treated WT mice (1818.49 ± 115.77 cells/mm^2; $p = 0.007$; Fig. 6k). The total number of RGCs in non-treated HET retinae was also significantly reduced compared to LT-treated WT mice (1654.32 ± 29.36 cells/mm^2; $p = 0.042$). A comparable

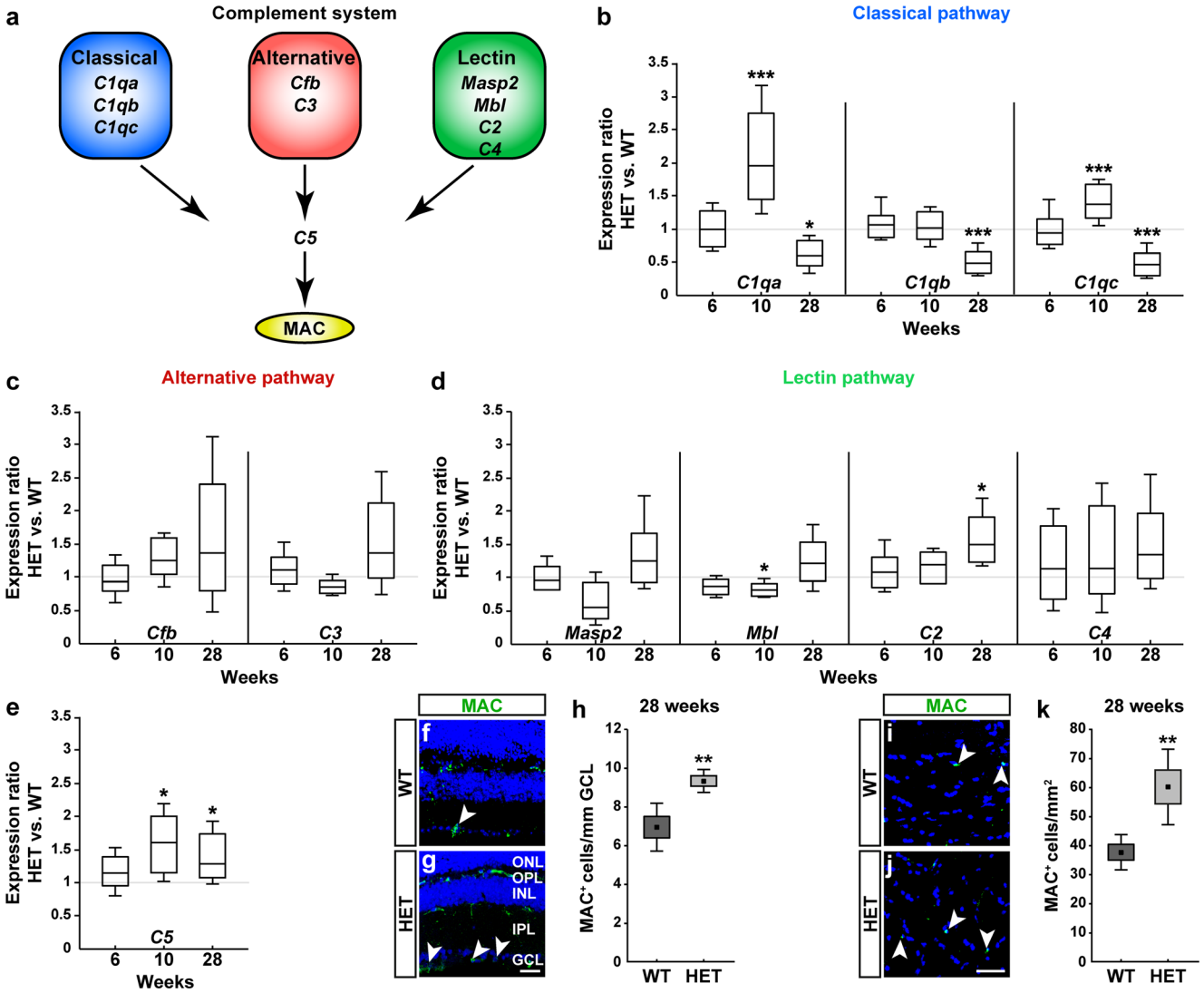

Fig. 5 *Meg2* HET mice exhibit early activation of the classical complement pathway. **a** Schematic illustration of investigated complement components associated with the classical, alternative, and lectin pathway. **b** At 28 weeks, RT-qPCR analyses ($n = 3$–4) revealed significantly reduced expression levels of the classical complement components *C1qa*, *C1qb*, and *C1qc* in HET retinae in comparison to WT littermates. At 10 weeks, *C1qa* and *C1qc* expression was significantly increased in HET retinae, whereas no change was observed for *C1qb* expression. No significant differences for *C1q* expression were observed at 6 weeks. **c** Regarding the alternative pathway, *Cfb* as well as *C3* expression was comparable at 28 weeks, 10 weeks, and 6 weeks in retinae of both genotypes. **d** For *Masp2* and *C4*, components of the lectin pathway, no dysregulation was found at all investigated points in time. At 10 weeks, a significantly lower *Mbl* expression level was observed in HET retinae. An increased *C2* level was noted at 28 weeks. **e** Still, the *C5* expression level was significantly increased in HET retinae at 28 and 10 weeks. **f**, **g** Immunohistochemical staining verified more MAC^+ deposits (green; arrowheads) in retinae of HET compared to WT mice at 28 weeks. **h** Counts revealed significantly more MAC^+ cells in the GCL of HET mice ($n = 5$). **i**–**k** Elevated numbers of MAC^+ cells (green; arrowheads) were also observed in HET optic nerves ($n = 5$). Nuclei were stained with TO-PRO-3 (blue). $^*p < 0.05$, $^{**}p < 0.01$, $^{***}p < 0.001$. Values in **b**–**e** are shown as median ± quartile ± min/max. Values in **h** and **k** are shown as mean ± SEM and SD. Scale bars = 20 μm in **g** and 20 μm in **j**. GCL ganglion cell layer, INL inner nuclear layer, IPL inner plexiform layer, ONL outer nuclear layer, OPL outer plexiform layer

number of RGCs were found in WT, LT-treated WT, as well as LT-treated HET retinae (1533.70 ± 89.88 cells/mm^2; $p > 0.05$). However, no difference in the total number of RGCs was observed between non-treated HET and LT-treated HET mice ($p = 0.17$). Equal numbers of $Brn3a^+$ RGCs were found in the central part of WT and HET retinae, suggesting that central RGC loss occurs later in HET mice ($p > 0.05$; Fig. 6l). In contrast, we revealed major differences between the groups in peripheral retinae (Fig. 6m). Here, a significantly reduced number of peripheral RGCs were observed in retinae of non-treated HET animals (1101.30 ± 44.59 cells/mm^2) in comparison to non-treated WT mice (1680.73 ± 49.56 cells/mm^2; $p < 0.001$). The number of RGCs in non-treated HET mice was significantly reduced compared to LT-treated HET animals (1410.33 ± 31.82 cells/mm^2; $p < 0.01$), indicating RGC protection. Similarly, the

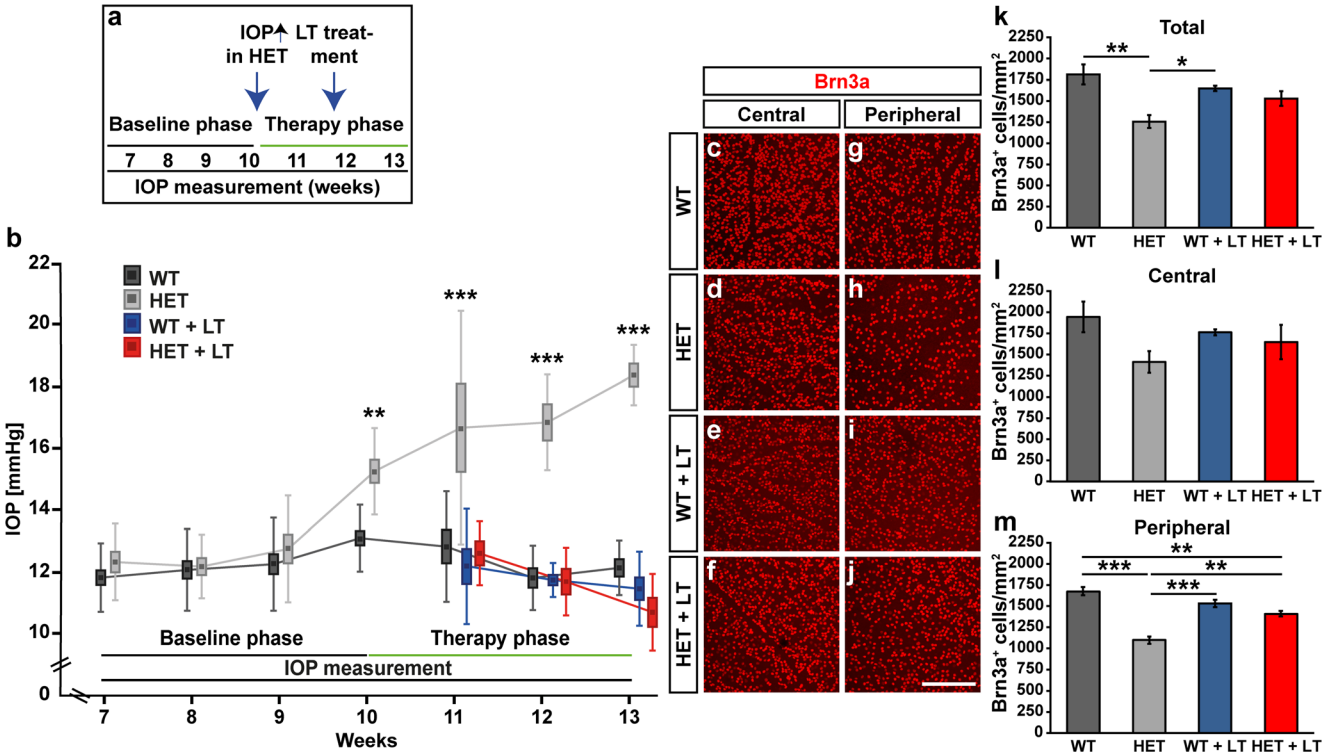

Fig. 6 Latanoprost lowers IOP and protects RGCs in *Meg2* HET mice. **a** Experimental design of the latanoprost (LT) treatment experiment. **b** *Meg2* HET mice developed progressive IOP elevation upon 10 weeks (end of baseline phase; baseline phase: $n = 14–22$; therapy phase: $n = 7–11$). Following LT treatment, HET mice exhibited a reduced IOP elevation (start therapy phase). In contrast, non-treated HET mice displayed progressive IOP elevation with ongoing experimental time. No changes were observed in control and LT-treated WT littermates. **c–j** Representative photographs show Brn3a$^+$ RGCs (red) in the central and peripheral flat-mount retina of non-treated and LT-treated WT and HET mice. **k–m** Quantification of total, central, and peripheral Brn3a$^+$ RGCs in non-treated and LT-treated WT and HET retinae ($n = 3$). HET animals exhibited a significant loss of total and peripheral Brn3a$^+$ RGCs in comparison to WT mice. No significant difference in the number of Brn3a$^+$ cells was found in the central retina of WT and HET mice. After LT treatment, no significant differences were noted between WT and HET animals. *$p < 0.05$, **$p < 0.01$, ***$p < 0.001$. Values in **b** are shown as mean ± SEM and SD. Values in **k–m** are shown as mean ± SEM. Scale bar = 100 μm in **j**

number of peripheral RGCs in non-treated HET animals was significantly reduced compared to LT-treated WT mice (1535.67 ± 44.49 cells/mm^2; $p < 0.001$). Also, the number of peripheral RGCs was significantly lower in LT-treated HET compared to non-treated WT retinae ($p < 0.01$), suggesting that LT therapy leads not to a complete rescue of RGCs in HET mice. Furthermore, we analyzed microglia in central (Figure S6a-d) and peripheral parts (Figure S6e-h) of HET and WT retinae following LT treatment. A significant increase in the total number of retinal Iba1$^+$ cells was observed in non-treated HET (243.20 ± 11.27 cells/mm^2) in comparison to WT (182.70 ± 7.60 cells/mm^2), LT-treated WT (183.68 ± 17.03 cells/mm^2), and LT-treated HET (169.89 ± 14.20 cells/mm^2; $p < 0.05$; Figure S6i) mice. Additionally, in the central area of the retinae, a significantly higher number of Iba1$^+$ microglia were noted in non-treated HET (248.33 ± 17.11 cells/mm^2) compared to WT (179.74 ± 11.65 cells/mm^2), LT-treated WT (180.13 ± 14.49 cells/mm^2), and LT-treated HET (173.83 ± 9.03 cells/mm^2; $p < 0.05$; Figure S6j) mice. Regarding the number of peripheral microglia, no significant change was found between WT (185.66 ± 6.51 cells/mm^2) and HET (238.08 ± 5.48 cells/mm^2; $p = 0.122$) mice and between LT-treated WT (187.23 ± 19.61 cells/mm^2) and HET (238.08 ± 5.48 cells/mm^2; $p = 0.136$; Figure S6k) mice. Most interestingly, in the peripheral retina of LT-treated HET (165.94 ± 19.36 cells/mm^2), a significantly lower number of microglia were observed compared to non-treated HET mice (238.08 ± 5.48 cells/mm^2; $p = 0.031$), indicating less microglial infiltration.

Meg2 HET Mice Show an Impairment of Retinal Functionality

Finally, we examined overall retinal function in HET mice. Therefore, ERG recordings were conducted in both groups at 1 year (Fig. 7a, b; Table S7). Under scotopic conditions, a-wave responses arise almost exclusively from rod-photoreceptors, while b-wave responses primarily arise from rod-bipolar and Müller glial cells. In both genotypes, a- and b-wave responses increased with higher light flash intensities. Nevertheless, compared to WT mice, HET animals exhibited significantly reduced a- and b-wave amplitudes ($p < 0.05$;

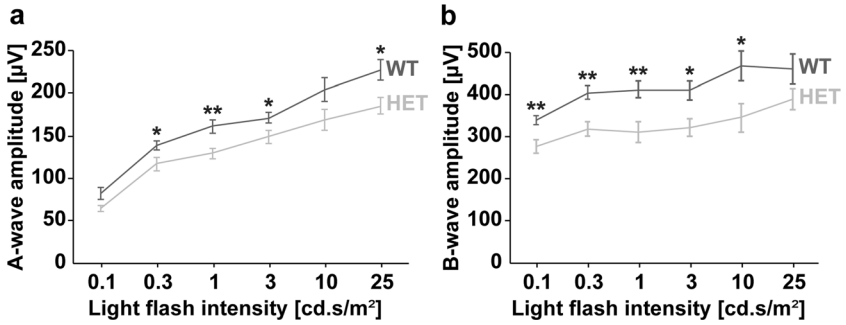

Fig. 7 Retinal dysfunction in *Meg2* HET mice. **a**, **b** ERG recordings from WT (black dashes) and *Meg2* HET (gray dashes) mice performed under scotopic conditions at 1 year ($n = 4$). Light flash intensities (cd.s/m^2) are indicated. Light intensities were plotted versus the amplitude size (µV). *Meg2* HET mice showed impaired ERG responses. Both, a- and b-wave amplitudes, were significantly reduced in *Meg2* HET mice, indicating retinal dysfunction. *$p < 0.05$, **$p < 0.01$. Values are shown as mean ± SEM. µV micro volt, cd candela

Fig. 7a, b), suggesting an impairment of retinal functionality. To examine retinal functionality at an earlier point in time, we also performed ERG recordings at 28 weeks of age (Table S7). However, only minor changes in the a-wave amplitude, but no changes in the b-wave amplitude were observed in HET compared to WT mice. This indicates a more pronounced impairment of retinal functionality with ongoing glaucomatous retinal degeneration.

Discussion

Mouse models represent powerful tools to investigate the molecular mechanisms contributing to multifactorial neurodegenerative diseases such as glaucoma [56–59]. In our study, we comprehensively analyzed the ocular phenotype of transgenic *Meg2*-deficient mice. Using a global microarray approach and RT-qPCR analyses, we detected a dysregulation of several candidate genes highly associated with retinal neurodegeneration in KO and HET retinae. Accordingly, we found out that HET mice exhibit progressive IOP elevation, optic nerve damage, and RGC loss. In addition, neurodegeneration in HET animals was accompanied by micro- and macroglial reactivity as well as complement activation. Through treatment with the anti-glaucomatous drug latanoprost, a significant IOP reduction, RGC protection, as well as reduced immigration of microglia could be achieved. Due to our findings, we propose that *Meg2* HET mice may serve as a novel animal model to unveil the molecular mechanisms involved in the onset and progression of glaucomatous neurodegeneration. To our knowledge, this is the first report of a glaucoma phenotype in a PTP-deficient animal.

On the molecular level, microarray and RT-qPCR analyses revealed a dysregulation of several retinal genes whose up- or downregulation correlates with glaucomatous and retinal degeneration, but also human pathogenesis. For example, *glutamate ionotropic receptor delta type subunit 2* (*Grid2*) was described as an underlying disease gene of early-onset autosomal recessive cerebellar ataxia and retinal dystrophy. Grid2 protein has been localized not only in photoreceptor cells but also in the GCL [60]. Since Grid2 is a member of the family of excitatory ionotropic glutamate receptors, the upregulation of *Grid2* in HET retinae could be related to glaucomatous glutamate-mediated excitotoxicity and death of RGCs [61, 62]. As in HET retinae, an increased expression of *insulin-like growth factor binding protein 3* (*Igfbp3*) has also been observed in the vitreous of patients with ischemic central retinal vein occlusion followed by secondary glaucoma [63]. In this regard, retinal endothelial cell-expressed Igfbp3 could display compensatory protective effects on the retinal vasculature in HET animals [64–66]. In our glaucomatous model, *ADP-dependent glucokinase* (*Adpgk*) was significantly downregulated in the retina. Adpgk plays a key role in the mitochondrial oxidative metabolism, and its downregulation has been shown to inhibit oxidative signals as well as NF-kB-dependent gene expression [67, 68]. A contribution of the NF-kB pathway in acute glaucoma has previously been described by Chi et al. [69]. We verified an increased expression of the extracellular matrix molecule biglycan in HET retinae. Intense staining of biglycan has been described in nerve fiber-rich layers and blood vessels of the retina and optic nerve [70, 71]. Furthermore, *Bgn* expression is upregulated in the context of glaucomatous optic neuropathy [72, 73]. Thus, *Meg2*-deficient mice may represent a promising tool for the identification of novel disease-associated genes.

Additionally, HET mice display several characteristics of a valuable and independent genetic glaucoma-like animal model. Most importantly, IOP elevation occurs spontaneously and at a relatively constant level. Furthermore, increased IOP was found upon 10 weeks, which represents a very early point in time compared to other glaucoma mouse models; for instance in DBA/2J mice, increased IOP extends at a later point in time, from 6 to 16 months [74, 75]. By 2–3 months, DBA/2J mice still have a physiological IOP level. First signs of apoptotic RGC death can be observed at around 8–9 months [76].

This is a quite late point in time compared to HET mice, which already show a significant RGC loss at 14 weeks. Since HET and WT mice exhibit a comparable RGC number at 6 weeks, loss at later points in time seems to depend directly on IOP elevation, while RGC development is not disturbed in this model. We already verified RGC loss in HET mice shortly after detection of IOP elevation. This loss was most prominent in the peripheral retina, while no significant loss was revealed in the central area, suggesting that peripheral RGCs might be more sensitive to an elevated IOP. Several studies using experimental IOP elevation models have reported that peripheral RGCs are more susceptible to damage and that peripheral RGC loss is greater than the central loss [77–79]. Correspondingly, studies of the magno- and parvocellular system suggest that magnocellular RGCs might be more susceptible in glaucoma [80]. However, more recent evidence suggests equal damage of RGC subtypes, indicating no cell type-specific loss, but rather topological RGC degeneration [81–83]. Additionally, variation in RGC loss might be due to differences in the RGC density as well as genetic and environmental factors [84]. In glaucoma, RGC loss occurs mainly by apoptosis [85]. As a characteristic feature of apoptosis, nuclei shrinkage has been observed in various experimental models, including DBA/2J and *Myoc* mutant mice [83, 86–88]. Studies in an experimental monkey glaucoma model reported that the selective loss of RGCs is accompanied by previous cell shrinkage [89, 90]. We also verified RGC shrinkage in *Meg2* HET mice. Due to a correlation between soma and nucleus size, smaller nuclei in HET mice might indicate morphological changes preceding RGC death. At 28 weeks, approximately 39% fewer RGCs were observed in *Meg2* HET compared to WT mice. In DBA/2NNia mice, RGC loss starts between 12 and 15 months. At 18 months, around 46% of RGCs are lost when compared to C57BL/6 mice [91]. Most DBA/2J mice exhibit an IOP that is 6–7 mmHg higher than that in control mice [75]. In DBA/2J, IOP elevation starts approximately at 6 months. Similarly, IOP in HET mice is around 4–7 mmHg higher than that in WT mice, although IOP elevation was slightly milder and already observed at 10 weeks. Both, IOP elevation and RGC loss seem to occur earlier, but slightly milder, in the *Meg2* mouse model, which offers the possibility to monitor proceeding glaucomatous neurodegeneration on a comparatively mild level. Accordingly, the *Meg2* HET model most likely mirrors the sneak progression observed in human POAG, since our analyses revealed an open iridocorneal angle. Thus, our model has various features resembling human POAG. Regarding the impaired retinal function in HET mice, both a- and b-wave amplitudes were found to be reduced after chronic IOP elevation, suggesting that retinal neurodegeneration not only affects the inner retina. Both a- and b-wave ERG recordings were reported to vary in human and experimental glaucoma, and photoreceptors are adversely affected following IOP elevation [92, 93]. Likewise, loss of outer retinal function and circuitry alterations were observed in aged DBA/2J mice [94, 95].

Astrocytic activation was found to be one of the earliest events occurring in response to elevated IOP [96]. Indeed, astroglial activation can be observed as early as 2 h after raising IOP levels, even before apoptosis of RGCs is induced [97, 98]. Son and colleagues [99] reported that glaucomatous optic nerve injury involves early astrocytic reactivity. Our analyses showed increased macrogliosis in HET retinae and optic nerves at 28 weeks as well as in retinae at > 1 year of age. At 10 weeks, when IOP elevation was evident, first signs of macrogliosis were observed in HET retinae and optic nerves, indicating early glial response in both tissues. Furthermore, our analyses also revealed late and early microglial infiltration in HET retinae/optic nerves at > 1 year, 28 weeks, and 14 weeks, most prominently in the central retina, which might indicate microglial immigration through the optic nerve. While macrogliosis was noted at 10 weeks in HET retinae, enhanced numbers of microglia were not observed at this early point in time, suggesting that macroglia undergo gliosis earlier after IOP elevation.

We also showed a specific contribution of the classical complement pathway in the *Meg2* mouse model. Our microarray analyses revealed a dysregulation of *C1qs* in the KO retinae. In HET retinae, an early upregulation of *C1qa* and *C1qc* was detected at 10 weeks. Since RGC loss was not evident at this early point in time, complement activation seems to precede neuronal cell death. At 28 weeks, *C1q* expression was significantly decreased, implicating that C1q activation terminates when many RGCs are lost, although MAC activation was still observable at 28 weeks. Expression of *Cfb*, *C3*, *Masp2*, and *C4* was comparable in both genotypes at early and late points in time. Therefore, we speculate that the alternative and lectin pathways are much less or not involved in glaucomatous neurodegeneration in this model. As a cellular source of C1q, Müller glia, astrocytes [100], microglia [101], and RGCs themselves [51, 102] were reported. Still, C1q, C3, and C5 are synthesized by microglia in vitro [103]. Increased *C1q* and *C5* expression as well as enhanced MAC immunoreactivity in HET retinae might correlate with the increased microglial and astrocytic response as well as RGC loss. Activated microglial cells were reported to induce neurotoxic reactive astrocytes [104]. Since mice with a C1qa mutation are protected from glaucoma [53] and the absence of C1q ameliorates RGC and optic nerve degeneration in DBA/2NNia mice [105], it was assumed that activation of the classical complement pathway propagates RGC death, which might also contribute to glaucomatous damage in *Meg2* HET mice.

In this regard, recent findings suggest that early complement responses are induced directly as a result of IOP elevation and not secondary to RGC dysfunction or damage in glaucomatous DBA/2J mice [106]. Recently, C1q was described to propagate activation of microglia and neurodegeneration in a retinal ischemia/reperfusion model [107]. Importantly, Williams et al. [108] demonstrated that the inhibition of the classical complement cascade prevents early dendritic and synaptic degeneration in glaucoma. Due to this finding, classical complement activation in glaucomatous *Meg2*-deficient mice may also contribute to the degeneration of synapses prior to cell loss.

Anti-glaucoma medication acts in a neuroprotective way in DBA/2J mice [109] and in glaucomatous $Vav2^{-/-}/Vav3^{-/-}$ mice [110]. Also, in our model, latanoprost effectively lowered IOP, suggesting that HET mice exhibit an impaired aqueous humor outflow. Although our current findings do not address the underlying molecular mechanisms, the trabecular meshwork might require Meg2 function. However, most importantly, we revealed that RGC loss in HET mice depends on progressive IOP elevation since its reduction effectively prevents RGC loss and microglial infiltration.

Conclusions

Our findings demonstrate that the heterozygous elimination of *Meg2* is sufficient to cause IOP elevation, progressive optic nerve damage, and RGC loss in mice. In a future perspective, *Meg2* HET mice might represent an attractive and independent in vivo neurodegeneration model to explore the molecular mechanism underlying glaucoma disease. Additionally, *Meg2*-deficient mice may also represent a promising tool to develop novel therapies, to screen neuroprotective drugs, and to identify potential biomarkers.

Acknowledgements The authors thank Zülal Caka, Stephanie Chun, Anja Coenen, Holger Schlierenkamp, and Marion Voelzkow for their excellent technical assistance.

Funding Information This research was supported by the German Research Foundation (DFG: SFB 509 TPA10; FA 159/14-1). J. R. was supported by the Research School, Ruhr-University Bochum (DFG: GSC 98/1). S. W. was supported by the Konrad-Adenauer Foundation (200520593).

Compliance with Ethical Standards

Ethical Approval All animal experiments were conducted in compliance with the "Association for Research and Vision and Ophthalmology" statement for the use of animals in ophthalmic and vision research and were approved by the ethics committee for animal experiments by the state North-Rhine Westphalia, Germany. The study was supervised by the animal welfare commissioner of the Ruhr-University Bochum. All efforts were made to reduce the number of animals in the experiments.

Conflict of Interest The authors declare that they have no conflict of interest.

References

1. Tham YC, Li X, Wong TY, Quigley HA, Aung T, Cheng CY (2014) Global prevalence of glaucoma and projections of glaucoma burden through 2040: a systematic review and meta-analysis. Ophthalmology 121(11):2081–2090. https://doi.org/10.1016/j.ophtha.2014.05.013
2. Nickells RW, Howell GR, Soto I, John SW (2012) Under pressure: cellular and molecular responses during glaucoma, a common neurodegeneration with axonopathy. Annu Rev Neurosci 35:153–179. https://doi.org/10.1146/annurev.neuro.051508.135728
3. Cordeiro MF, Guo L, Luong V, Harding G, Wang W, Jones HE, Moss SE, Sillito AM et al (2004) Real-time imaging of single nerve cell apoptosis in retinal neurodegeneration. Proc Natl Acad Sci U S A 101(36):13352–13356. https://doi.org/10.1073/pnas.0405479101
4. Braunger BM, Fuchshofer R, Tamm ER (2015) The aqueous humor outflow pathways in glaucoma: a unifying concept of disease mechanisms and causative treatment. Eur J Pharm Biopharm 95(Pt B):173–181. https://doi.org/10.1016/j.ejpb.2015.04.029
5. Johnson EC, Morrison JC (2009) Friend or foe? Resolving the impact of glial responses in glaucoma. J Glaucoma 18(5):341–353. https://doi.org/10.1097/IJG.0b013e31818c6ef6
6. Tezel G (2009) The role of glia, mitochondria, and the immune system in glaucoma. Invest Ophthalmol Vis Sci 50(3):1001–1012. https://doi.org/10.1167/iovs.08-2717
7. Tezel G (2013) Immune regulation toward immunomodulation for neuroprotection in glaucoma. Curr Opin Pharmacol 13(1):23–31. https://doi.org/10.1016/j.coph.2012.09.013
8. Tezel G, Wax MB (2004) The immune system and glaucoma. Curr Opin Ophthalmol 15(2):80–84
9. Tezel G, Yang X, Luo C, Kain AD, Powell DW, Kuehn MH, Kaplan HJ (2010) Oxidative stress and the regulation of complement activation in human glaucoma. Invest Ophthalmol Vis Sci 51(10):5071–5082. https://doi.org/10.1167/iovs.10-5289
10. Tonks NK, Neel BG (1996) From form to function: signaling by protein tyrosine phosphatases. Cell 87(3):365–368
11. den Hertog J (1999) Protein-tyrosine phosphatases in development. Mech Dev 85 (1–2):3–14.
12. Alonso A, Sasin J, Bottini N, Friedberg I, Osterman A, Godzik A, Hunter T, Dixon J et al (2004) Protein tyrosine phosphatases in the human genome. Cell 117(6):699–711. https://doi.org/10.1016/j.cell.2004.05.018
13. Hale AJ, Ter Steege E, den Hertog J (2017) Recent advances in understanding the role of protein-tyrosine phosphatases in development and disease. Dev Biol 428(2):283–292. https://doi.org/10.1016/j.ydbio.2017.03.023
14. Julien SG, Dube N, Hardy S, Tremblay ML (2011) Inside the human cancer tyrosine phosphatome. Nat Rev Cancer 11(1):35–49. https://doi.org/10.1038/nrc2980
15. Tonks NK (2006) Protein tyrosine phosphatases: from genes, to function, to disease. Nat Rev Mol Cell Biol 7(11):833–846. https://doi.org/10.1038/nrm2039
16. Mustelin T, Vang T, Bottini N (2005) Protein tyrosine phosphatases and the immune response. Nat Rev Immunol 5(1):43–57. https://doi.org/10.1038/nri1530
17. Paul S, Lombroso PJ (2003) Receptor and nonreceptor protein tyrosine phosphatases in the nervous system. Cell Mol Life Sci 60(11):2465–2482. https://doi.org/10.1007/s00018-003-3123-7

18. Stoker AW (2015) RPTPs in axons, synapses and neurology. Semin Cell Dev Biol 37:90–97. https://doi.org/10.1016/j.semcdb.2014.09.006
19. Horvat-Brocker A, Reinhard J, Illes S, Paech T, Zoidl G, Harroch S, Distler C, Knyazev P et al (2008) Receptor protein tyrosine phosphatases are expressed by cycling retinal progenitor cells and involved in neuronal development of mouse retina. Neuroscience 152(3):618–645. https://doi.org/10.1016/j.neuroscience.2008.01.016
20. Reinhard J, Horvat-Brocker A, Illes S, Zaremba A, Knyazev P, Ullrich A, Faissner A (2009) Protein tyrosine phosphatases expression during development of mouse superior colliculus. Exp Brain Res 199(3–4):279–297. https://doi.org/10.1007/s00221-009-1963-6
21. Gu M, Warshawsky I, Majerus PW (1992) Cloning and expression of a cytosolic megakaryocyte protein-tyrosine-phosphatase with sequence homology to retinaldehyde-binding protein and yeast SEC14p. Proc Natl Acad Sci U S A 89(7):2980–2984
22. Huang X, Gschweng E, Van Handel B, Cheng D, Mikkola HK, Witte ON (2011) Regulated expression of microRNAs-126/126* inhibits erythropoiesis from human embryonic stem cells. Blood 117(7):2157–2165. https://doi.org/10.1182/blood-2010-08-302711
23. Xu MJ, Sui X, Zhao R, Dai C, Krantz SB, Zhao ZJ (2003) PTP-MEG2 is activated in polycythemia vera erythroid progenitor cells and is required for growth and expansion of erythroid cells. Blood 102(13):4354–4360. https://doi.org/10.1182/blood-2003-04-1308
24. Huynh H, Bottini N, Williams S, Cherepanov V, Musumeci L, Saito K, Bruckner S, Vachon E et al (2004) Control of vesicle fusion by a tyrosine phosphatase. Nat Cell Biol 6(9):831–839. https://doi.org/10.1038/ncb1164
25. Saito K, Williams S, Bulankina A, Honing S, Mustelin T (2007) Association of protein-tyrosine phosphatase MEG2 via its Sec14p homology domain with vesicle-trafficking proteins. J Biol Chem 282(20):15170–15178. https://doi.org/10.1074/jbc.M608682200
26. Wang Y, Vachon E, Zhang J, Cherepanov V, Kruger J, Li J, Saito K, Shannon P et al (2005) Tyrosine phosphatase MEG2 modulates murine development and platelet and lymphocyte activation through secretory vesicle function. J Exp Med 202(11):1587–1597. https://doi.org/10.1084/jem.20051108
27. Huynh H, Wang X, Li W, Bottini N, Williams S, Nika K, Ishihara H, Godzik A et al (2003) Homotypic secretory vesicle fusion induced by the protein tyrosine phosphatase MEG2 depends on polyphosphoinositides in T cells. J Immunol 171(12):6661–6671
28. D'Amour KA, Gage FH (2003) Genetic and functional differences between multipotent neural and pluripotent embryonic stem cells. Proc Natl Acad Sci U S A 100(Suppl 1):11866–11872. https://doi.org/10.1073/pnas.1834200100
29. Zhang D, Marlin MC, Liang Z, Ahmad M, Ashpole NM, Sonntag WE, Zhao ZJ, Li G (2016) The protein tyrosine phosphatase MEG2 regulates the transport and signal transduction of tropomyosin receptor kinase a. J Biol Chem 291(46):23895–23905. https://doi.org/10.1074/jbc.M116.728550
30. Curwin AJ, McMaster CR (2008) Structure and function of the enigmatic Sec14 domain-containing proteins and the etiology of human disease. Future Lipidol 3(4):399–410. https://doi.org/10.2217/17460875.3.4.399
31. Reinehr S, Reinhard J, Gandej M, Kuehn S, Noristani R, Faissner A, Dick HB, Joachim SC (2016) Simultaneous complement response via lectin pathway in retina and optic nerve in an experimental autoimmune glaucoma model. Front Cell Neurosci 10:140. https://doi.org/10.3389/fncel.2016.00140
32. Reinhard J, Renner M, Wiemann S, Shakoor DA, Stute G, Dick HB, Faissner A, Joachim SC (2017) Ischemic injury leads to extracellular matrix alterations in retina and optic nerve. Sci Rep 7:43470. https://doi.org/10.1038/srep43470
33. Luft V, Reinhard J, Shibuya M, Fischer KD, Faissner A (2015) The guanine nucleotide exchange factor Vav3 regulates differentiation of progenitor cells in the developing mouse retina. Cell Tissue Res 359(2):423–440. https://doi.org/10.1007/s00441-014-2050-2
34. Pfaffl MW, Horgan GW, Dempfle L (2002) Relative expression software tool (REST) for group-wise comparison and statistical analysis of relative expression results in real-time PCR. Nucleic Acids Res 30(9):e36
35. Gentleman RC, Carey VJ, Bates DM, Bolstad B, Dettling M, Dudoit S, Ellis B, Gautier L et al (2004) Bioconductor: open software development for computational biology and bioinformatics. Genome Biol 5(10):R80. https://doi.org/10.1186/gb-2004-5-10-r80
36. Irizarry RA, Hobbs B, Collin F, Beazer-Barclay YD, Antonellis KJ, Scherf U, Speed TP (2003) Exploration, normalization, and summaries of high density oligonucleotide array probe level data. Biostatistics 4(2):249–264. https://doi.org/10.1093/biostatistics/4.2.249
37. Schmid H, Renner M, Dick HB, Joachim SC (2014) Loss of inner retinal neurons after retinal ischemia in rats. Invest Ophthalmol Vis Sci 55(4):2777–2787. https://doi.org/10.1167/iovs.13-13372
38. Reinehr S, Reinhard J, Wiemann S, Stute G, Kuehn S, Woestmann J, Dick HB, Faissner A et al (2016) Early remodelling of the extracellular matrix proteins tenascin-C and phosphacan in retina and optic nerve of an experimental autoimmune glaucoma model. J Cell Mol Med 20(11):2122–2137. https://doi.org/10.1111/jcmm.12909
39. Almasieh M, Wilson AM, Morquette B, Cueva Vargas JL, Di Polo A (2012) The molecular basis of retinal ganglion cell death in glaucoma. Prog Retin Eye Res 31(2):152–181. https://doi.org/10.1016/j.preteyeres.2011.11.002
40. Nadal-Nicolas FM, Jimenez-Lopez M, Sobrado-Calvo P, Nieto-Lopez L, Canovas-Martinez I, Salinas-Navarro M, Vidal-Sanz M, Agudo M (2009) Brn3a as a marker of retinal ganglion cells: qualitative and quantitative time course studies in naive and optic nerve-injured retinas. Invest Ophthalmol Vis Sci 50(8):3860–3868. https://doi.org/10.1167/iovs.08-3267
41. Xiang M, Zhou H, Nathans J (1996) Molecular biology of retinal ganglion cells. Proc Natl Acad Sci U S A 93(2):596–601
42. Inman DM, Horner PJ (2007) Reactive nonproliferative gliosis predominates in a chronic mouse model of glaucoma. Glia 55(9):942–953. https://doi.org/10.1002/glia.20516
43. de Hoz R, Rojas B, Ramirez AI, Salazar JJ, Gallego BI, Trivino A, Ramirez JM (2016) Retinal macroglial responses in health and disease. Biomed Res Int 2016:2954721. https://doi.org/10.1155/2016/2954721
44. Bringmann A, Wiedemann P (2012) Muller glial cells in retinal disease. Ophthalmologica 227(1):1–19. https://doi.org/10.1159/000328979
45. Karlstetter M, Ebert S, Langmann T (2010) Microglia in the healthy and degenerating retina: insights from novel mouse models. Immunobiology 215(9–10):685–691. https://doi.org/10.1016/j.imbio.2010.05.010
46. Langmann T (2007) Microglia activation in retinal degeneration. J Leukoc Biol 81(6):1345–1351. https://doi.org/10.1189/jlb.0207114
47. Karlstetter M, Scholz R, Rutar M, Wong WT, Provis JM, Langmann T (2015) Retinal microglia: just bystander or target for therapy? Prog Retin Eye Res 45:30–57. https://doi.org/10.1016/j.preteyeres.2014.11.004
48. Ahmed F, Brown KM, Stephan DA, Morrison JC, Johnson EC, Tomarev SI (2004) Microarray analysis of changes in mRNA levels in the rat retina after experimental elevation of intraocular pressure. Invest Ophthalmol Vis Sci 45(4):1247–1258
49. Kuehn MH, Kim CY, Ostojic J, Bellin M, Alward WL, Stone EM, Sakaguchi DS, Grozdanic SD et al (2006) Retinal synthesis and

deposition of complement components induced by ocular hypertension. Exp Eye Res 83(3):620–628. https://doi.org/10.1016/j.exer.2006.03.002
50. Kuehn MH, Kim CY, Jiang B, Dumitrescu AV, Kwon YH (2008) Disruption of the complement cascade delays retinal ganglion cell death following retinal ischemia-reperfusion. Exp Eye Res 87(2):89–95. https://doi.org/10.1016/j.exer.2008.04.012
51. Stasi K, Nagel D, Yang X, Wang RF, Ren L, Podos SM, Mittag T, Danias J (2006) Complement component 1Q (C1Q) upregulation in retina of murine, primate, and human glaucomatous eyes. Invest Ophthalmol Vis Sci 47(3):1024–1029. https://doi.org/10.1167/iovs.05-0830
52. Ren L, Danias J (2010) A role for complement in glaucoma? Adv Exp Med Biol 703:95–104. https://doi.org/10.1007/978-1-4419-5635-4_7
53. Howell GR, Macalinao DG, Sousa GL, Walden M, Soto I, Kneeland SC, Barbay JM, King BL et al (2011) Molecular clustering identifies complement and endothelin induction as early events in a mouse model of glaucoma. J Clin Invest 121(4):1429–1444. https://doi.org/10.1172/JCI44646
54. Jha P, Banda H, Tytarenko R, Bora PS, Bora NS (2011) Complement mediated apoptosis leads to the loss of retinal ganglion cells in animal model of glaucoma. Mol Immunol 48(15–16):2151–2158. https://doi.org/10.1016/j.molimm.2011.07.012
55. Howell GR, Soto I, Ryan M, Graham LC, Smith RS, John SW (2013) Deficiency of complement component 5 ameliorates glaucoma in DBA/2J mice. J Neuroinflammation 10:76. https://doi.org/10.1186/1742-2094-10-76
56. John SW, Anderson MG, Smith RS (1999) Mouse genetics: a tool to help unlock the mechanisms of glaucoma. J Glaucoma 8(6):400–412
57. Weinreb RN, Lindsey JD (2005) The importance of models in glaucoma research. J Glaucoma 14(4):302–304
58. McKinnon SJ, Schlamp CL, Nickells RW (2009) Mouse models of retinal ganglion cell death and glaucoma. Exp Eye Res 88(4):816–824. https://doi.org/10.1016/j.exer.2008.12.002
59. Pang IH, Clark AF (2007) Rodent models for glaucoma retinopathy and optic neuropathy. J Glaucoma 16(5):483–505. https://doi.org/10.1097/IJG.0b013e3181405d4f
60. Van Schil K, Meire F, Karlstetter M, Bauwens M, Verdin H, Coppieters F, Scheiffert E, Van Nechel C et al (2015) Early-onset autosomal recessive cerebellar ataxia associated with retinal dystrophy: new human hotfoot phenotype caused by homozygous GRID2 deletion. Genet Med 17(4):291–299. https://doi.org/10.1038/gim.2014.95
61. Cheung W, Guo L, Cordeiro MF (2008) Neuroprotection in glaucoma: drug-based approaches. Optom Vis Sci 85(6):406–416. https://doi.org/10.1097/OPX.0b013e31817841e5
62. Sucher NJ, Lipton SA, Dreyer EB (1997) Molecular basis of glutamate toxicity in retinal ganglion cells. Vis Res 37(24):3483–3493. https://doi.org/10.1016/S0042-6989(97)00047-3
63. Ehlken C, Grundel B, Michels D, Junker B, Stahl A, Schlunck G, Hansen LL, Feltgen N et al (2015) Increased expression of angiogenic and inflammatory proteins in the vitreous of patients with ischemic central retinal vein occlusion. PLoS One 10(5):e0126859. https://doi.org/10.1371/journal.pone.0126859
64. Zhang Q, Jiang Y, Toutounchian JJ, Soderland C, Yates CR, Steinle JJ (2013) Insulin-like growth factor binding protein-3 inhibits monocyte adhesion to retinal endothelial cells in high glucose conditions. Mol Vis 19:796–803
65. Jiang Y, Zhang Q, Steinle JJ (2014) Intravitreal injection of IGFBP-3 restores normal insulin signaling in diabetic rat retina. PLoS One 9(4):e93788. https://doi.org/10.1371/journal.pone.0093788
66. Jiang Y, Pagadala J, Miller DD, Steinle JJ (2014) Insulin-like growth factor-1 binding protein 3 (IGFBP-3) promotes recovery from trauma-induced expression of inflammatory and apoptotic factors in retina. Cytokine 70(2):115–119. https://doi.org/10.1016/j.cyto.2014.07.004
67. Richter S, Morrison S, Connor T, Su J, Print CG, Ronimus RS, McGee SL, Wilson WR (2013) Zinc finger nuclease mediated knockout of ADP-dependent glucokinase in cancer cell lines: effects on cell survival and mitochondrial oxidative metabolism. PLoS One 8(6):e65267. https://doi.org/10.1371/journal.pone.0065267
68. Kaminski MM, Sauer SW, Kaminski M, Opp S, Ruppert T, Grigaravicius P, Grudnik P, Grone HJ et al (2012) T cell activation is driven by an ADP-dependent glucokinase linking enhanced glycolysis with mitochondrial reactive oxygen species generation. Cell Rep 2(5):1300–1315. https://doi.org/10.1016/j.celrep.2012.10.009
69. Chi W, Chen H, Li F, Zhu Y, Yin W, Zhuo Y (2015) HMGB1 promotes the activation of NLRP3 and caspase-8 inflammasomes via NF-kappaB pathway in acute glaucoma. J Neuroinflammation 12:137. https://doi.org/10.1186/s12974-015-0360-2
70. Ali SA, Hosaka YZ, Uehara M (2011) Spatiotemporal distribution of chondroitin sulfate proteoglycans in the developing mouse retina and optic nerve. J Vet Med Sci 73(1):13–18
71. Keenan TD, Clark SJ, Unwin RD, Ridge LA, Day AJ, Bishop PN (2012) Mapping the differential distribution of proteoglycan core proteins in the adult human retina, choroid, and sclera. Invest Ophthalmol Vis Sci 53(12):7528–7538. https://doi.org/10.1167/iovs.12-10797
72. Kirwan RP, Fenerty CH, Crean J, Wordinger RJ, Clark AF, O'Brien CJ (2005) Influence of cyclical mechanical strain on extracellular matrix gene expression in human lamina cribrosa cells in vitro. Mol Vis 11:798–810
73. Kirwan RP, Leonard MO, Murphy M, Clark AF, O'Brien CJ (2005) Transforming growth factor-beta-regulated gene transcription and protein expression in human GFAP-negative lamina cribrosa cells. Glia 52(4):309–324. https://doi.org/10.1002/glia.20247
74. John SW, Smith RS, Savinova OV, Hawes NL, Chang B, Turnbull D, Davisson M, Roderick TH et al (1998) Essential iris atrophy, pigment dispersion, and glaucoma in DBA/2J mice. Invest Ophthalmol Vis Sci 39(6):951–962
75. Libby RT, Anderson MG, Pang IH, Robinson ZH, Savinova OV, Cosma IM, Snow A, Wilson LA et al (2005) Inherited glaucoma in DBA/2J mice: pertinent disease features for studying the neurodegeneration. Vis Neurosci 22(5):637–648. https://doi.org/10.1017/S0952523805225130
76. Nagaraju M, Saleh M, Porciatti V (2007) IOP-dependent retinal ganglion cell dysfunction in glaucomatous DBA/2J mice. Invest Ophthalmol Vis Sci 48(10):4573–4579. https://doi.org/10.1167/iovs.07-0582
77. Laquis S, Chaudhary P, Sharma SC (1998) The patterns of retinal ganglion cell death in hypertensive eyes. Brain Res 784(1–2):100–104
78. Urcola JH, Hernandez M, Vecino E (2006) Three experimental glaucoma models in rats: comparison of the effects of intraocular pressure elevation on retinal ganglion cell size and death. Exp Eye Res 83(2):429–437. https://doi.org/10.1016/j.exer.2006.01.025
79. Chen H, Wei X, Cho KS, Chen G, Sappington R, Calkins DJ, Chen DF (2011) Optic neuropathy due to microbead-induced elevated intraocular pressure in the mouse. Invest Ophthalmol Vis Sci 52(1):36–44. https://doi.org/10.1167/iovs.09-5115
80. Quigley HA, Sanchez RM, Dunkelberger GR, L'Hernault NL, Baginski TA (1987) Chronic glaucoma selectively damages large optic nerve fibers. Invest Ophthalmol Vis Sci 28(6):913–920
81. Battista J, Badcock DR, McKendrick AM (2009) Spatial summation properties for magnocellular and parvocellular pathways in glaucoma. Invest Ophthalmol Vis Sci 50(3):1221–1226. https://doi.org/10.1167/iovs.08-2517

82. Yucel YH, Zhang Q, Weinreb RN, Kaufman PL, Gupta N (2003) Effects of retinal ganglion cell loss on magno-, parvo-, koniocellular pathways in the lateral geniculate nucleus and visual cortex in glaucoma. Prog Retin Eye Res 22(4):465–481
83. Jakobs TC, Libby RT, Ben Y, John SW, Masland RH (2005) Retinal ganglion cell degeneration is topological but not cell type specific in DBA/2J mice. J Cell Biol 171(2):313–325. https://doi.org/10.1083/jcb.200506099
84. Williams RW, Strom RC, Rice DS, Goldowitz D (1996) Genetic and environmental control of variation in retinal ganglion cell number in mice. J Neurosci 16(22):7193–7205
85. Quigley HA (1999) Neuronal death in glaucoma. Prog Retin Eye Res 18(1):39–57
86. Senatorov V, Malyukova I, Fariss R, Wawrousek EF, Swaminathan S, Sharan SK, Tomarev S (2006) Expression of mutated mouse myocilin induces open-angle glaucoma in transgenic mice. J Neurosci 26(46):11903–11914. https://doi.org/10.1523/JNEUROSCI.3020-06.2006
87. Rogalinska M (2002) Alterations in cell nuclei during apoptosis. Cell Mol Biol Lett 7(4):995–1018
88. Nickells RW (2012) The cell and molecular biology of glaucoma: mechanisms of retinal ganglion cell death. Invest Ophthalmol Vis Sci 53(5):2476–2481. https://doi.org/10.1167/iovs.12-9483h
89. Morgan JE, Uchida H, Caprioli J (2000) Retinal ganglion cell death in experimental glaucoma. Br J Ophthalmol 84(3):303–310
90. Morgan JE (2002) Retinal ganglion cell shrinkage in glaucoma. J Glaucoma 11(4):365–370
91. Danias J, Lee KC, Zamora MF, Chen B, Shen F, Filippopoulos T, Su Y, Goldblum D et al (2003) Quantitative analysis of retinal ganglion cell (RGC) loss in aging DBA/2NNia glaucomatous mice: comparison with RGC loss in aging C57/BL6 mice. Invest Ophthalmol Vis Sci 44(12):5151–5162
92. Pelzel HR, Schlamp CL, Poulsen GL, Ver Hoeve JA, Nork TM, Nickells RW (2006) Decrease of cone opsin mRNA in experimental ocular hypertension. Mol Vis 12:1272–1282
93. Velten IM, Korth M, Horn FK (2001) The a-wave of the dark adapted electroretinogram in glaucomas: are photoreceptors affected? Br J Ophthalmol 85(4):397–402
94. Heiduschka P, Julien S, Schuettauf F, Schnichels S (2010) Loss of retinal function in aged DBA/2J mice—new insights into retinal neurodegeneration. Exp Eye Res 91(5):779–783. https://doi.org/10.1016/j.exer.2010.09.001
95. Fernandez-Sanchez L, de Sevilla Muller LP, Brecha NC, Cuenca N (2014) Loss of outer retinal neurons and circuitry alterations in the DBA/2J mouse. Invest Ophthalmol Vis Sci 55(9):6059–6072. https://doi.org/10.1167/iovs.14-14421
96. Johnson EC, Deppmeier LM, Wentzien SK, Hsu I, Morrison JC (2000) Chronology of optic nerve head and retinal responses to elevated intraocular pressure. Invest Ophthalmol Vis Sci 41(2):431–442
97. Woldemussie E, Wijono M, Ruiz G (2004) Muller cell response to laser-induced increase in intraocular pressure in rats. Glia 47(2):109–119. https://doi.org/10.1002/glia.20000
98. Kanamori A, Nakamura M, Nakanishi Y, Yamada Y, Negi A (2005) Long-term glial reactivity in rat retinas ipsilateral and contralateral to experimental glaucoma. Exp Eye Res 81(1):48–56. https://doi.org/10.1016/j.exer.2005.01.012
99. Son JL, Soto I, Oglesby E, Lopez-Roca T, Pease ME, Quigley HA, Marsh-Armstrong N (2010) Glaucomatous optic nerve injury involves early astrocyte reactivity and late oligodendrocyte loss. Glia 58(7):780–789. https://doi.org/10.1002/glia.20962
100. Kishore U, Reid KB (2000) C1q: structure, function, and receptors. Immunopharmacology 49(1–2):159–170
101. Fonseca MI, Chu SH, Hernandez MX, Fang MJ, Modarresi L, Selvan P, MacGregor GR, Tenner AJ (2017) Cell-specific deletion of C1qa identifies microglia as the dominant source of C1q in mouse brain. J Neuroinflammation 14(1):48. https://doi.org/10.1186/s12974-017-0814-9
102. Stevens B, Allen NJ, Vazquez LE, Howell GR, Christopherson KS, Nouri N, Micheva KD, Mehalow AK et al (2007) The classical complement cascade mediates CNS synapse elimination. Cell 131(6):1164–1178. https://doi.org/10.1016/j.cell.2007.10.036
103. Luo C, Chen M, Xu H (2011) Complement gene expression and regulation in mouse retina and retinal pigment epithelium/choroid. Mol Vis 17:1588–1597
104. Liddelow SA, Guttenplan KA, Clarke LE, Bennett FC, Bohlen CJ, Schirmer L, Bennett ML, Munch AE et al (2017) Neurotoxic reactive astrocytes are induced by activated microglia. Nature 541(7638):481–487. https://doi.org/10.1038/nature21029
105. Kumari R, Astafurov K, Genis A, Danias J (2015) Differential effects of C1qa ablation on glaucomatous damage in two sexes in DBA/2NNia mice. PLoS One 10(11):e0142199. https://doi.org/10.1371/journal.pone.0142199
106. Harder JM, Braine CE, Williams PA, Zhu X, MacNicoll KH, Sousa GL, Buchanan RA, Smith RS et al (2017) Early immune responses are independent of RGC dysfunction in glaucoma with complement component C3 being protective. Proc Natl Acad Sci U S A 114(19):E3839–E3848. https://doi.org/10.1073/pnas.1608769114
107. Silverman SM, Kim BJ, Howell GR, Miller J, John SW, Wordinger RJ, Clark AF (2016) C1q propagates microglial activation and neurodegeneration in the visual axis following retinal ischemia/reperfusion injury. Mol Neurodegener 11:24. https://doi.org/10.1186/s13024-016-0089-0
108. Williams PA, Tribble JR, Pepper KW, Cross SD, Morgan BP, Morgan JE, John SW, Howell GR (2016) Inhibition of the classical pathway of the complement cascade prevents early dendritic and synaptic degeneration in glaucoma. Mol Neurodegener 11:26. https://doi.org/10.1186/s13024-016-0091-6
109. Schuettauf F, Quinto K, Naskar R, Zurakowski D (2002) Effects of anti-glaucoma medications on ganglion cell survival: the DBA/2J mouse model. Vis Res 42(20):2333–2337
110. Fujikawa K, Iwata T, Inoue K, Akahori M, Kadotani H, Fukaya M, Watanabe M, Chang Q et al (2010) VAV2 and VAV3 as candidate disease genes for spontaneous glaucoma in mice and humans. PLoS One 5(2):e9050. https://doi.org/10.1371/journal.pone.0009050